HHS Public Access

Author manuscript

J Am Chem Soc. Author manuscript; available in PMC 2017 July 20.

Published in final edited form as:

J Am Chem Soc. 2017 January 11; 139(1): 293–310. doi:10.1021/jacs.6b10744.

Chemomechanical coupling in hexameric protein-protein interfaces harness energy within V–type ATPases

Abhishek Singharoy[†], **Christophe Chipot**[‡,†,¶], **Mahmoud Moradi**[§], and **Klaus Schulten**[†,¶]

[†]Theoretical and Computational Biophysics Group, Beckman Institute for Advanced Science and Technology, University of Illinois at Urbana-Champaign, 405 North Mathews Avenue, Urbana, Illinois 61801

[‡]Laboratoire International Associé Centre National de la Recherche Scientifique et University of Illinois at Urbana-Champaign, Unité Mixte de Recherche n°7565, Université de Lorraine, B.P. 70239, 54506 Vandoeuvre-lès-Nancy cedex, France

[¶]Department of Physics, University of Illinois at Urbana-Champaign, 1110 West Green Street, Urbana, Illinois 61801

[§]Department of Chemistry and Biochemistry, University of Arkansas, Fayetteville, Arkansas 72701

Abstract

ATP synthase is the most prominent bioenergetic macromolecular motor in all life-forms, utilizing the proton gradient across the cell membrane to fuel the synthesis of ATP. Notwithstanding the wealth of available biochemical and structural information inferred from years of experiments, the precise molecular mechanism whereby vacuolar (V–type) ATP synthase fulfills its biological function remains largely fragmentary. Recently, crystallographers provided the first high-resolution view of ATP activity in *Enterococcus hirae* V_1–ATPase. Employing a combination of transition-path sampling and high-performance free-energy methods, the sequence of conformational transitions involved in a functional cycle accompanying ATP hydrolysis has been investigated in unprecedented detail over an aggregate simulation time of 65 μs. Our simulated pathways reveal that the chemical energy produced by ATP hydrolysis is harnessed via the concerted motion of the protein–protein interfaces in the V_1-ring, and is nearly entirely consumed in the rotation of the central stalk. Surprisingly, in an ATPase devoid of a central stalk, the interfaces of this ring are perfectly designed for inducing ATP hydrolysis. Yet, in a complete V_1-ATPase, the mechanical property of the central stalk is a key determinant of the rate of ATP turnover. The simulations further unveil a sequence of events, whereby unbinding of the hydrolysis product (ADP+P_i) is followed by ATP uptake, which, in turn, leads to the torque generation step and rotation of the center stalk. Molecular trajectories also bring to light multiple intermediates, two of which have been isolated in independent crystallography experiments.

Correspondence to: Klaus Schulten.

Supporting Information Available

This material is available free of charge via the Internet at http://pubs.acs.org/.

Introduction

F_oF_1–ATPase, also known as ATP synthase, is a motor protein that harnesses energy from the translocation of protons across biological membranes and utilizes the energy towards synthesis or hydrolysis of ATP. Given that ATP is the universal carrier of energy in all living systems, ATP synthase serves as a ubiquitous, evolutionary conserved enzyme, present in bacterial cell membranes, thylakoid membranes of chloroplasts, as well as the inner membrane of mitochondria. A second class of ATPases, vacoular or V–ATPases, are thought to have originated from an ancestral enzyme in common with F–ATPases.[1] The main function of V–ATPases in eukaryotes is to transport protons across the membrane by using the energy produced by ATP hydrolysis.[2] V–ATPases also catalyze ATP synthesis, exploiting the energy of proton flow in certain eubacteria, such as *Thermus thermophilus*.

Crystallographic studies reveal that both F- and V- forms of ATPases possess an overall similar three–dimensional structure, composed of a hydrophilic domain (V_1 and F_1) and a membrane– embedded, ion–transporting domain (V_o and F_o) connected by central and peripheral stalk(s). The F_1 domain consists of a ring that includes three copies of an $\alpha\beta$ subunit, forming an $\alpha_3\beta_3$ complex, and a central stalk with a γ and a δ subunit.[2] Likewise, the V_1 domain consists of an A_3B_3 ring and a central DF stalk (Figure 1).[1] Furthermore, both ATPases follow a similar ATP synthesis/hydrolysis mechanism. Coined rotatory–catalysis,[3–5] the chemical reactions occur through conformational rotation of the ring and physical rotation of the central stalk.[3–5]

Notwithstanding structural similarities, single–molecule experiments reveal stark contrasts in the detail of the rotatory–catalysis steps in F_1– and V_1–ATPases: While rotation in F_1 involves three sub–steps,[6] V_1–ATPase does not involve any sub–step during rotation.[7] The sequence identity between the two ATPases only ranges between 20 and 30 %.[8] Last, the rotatory–catalysis efficiency in F_1 is higher than that in V_1.[2] However, even with the plethora of available structural and biochemical information, molecular mechanisms delineating the similarities and differences between the motor-action of F– and V–type ATPases remain unresolved.

Boyer developed a binding–change model which postulated that ATP synthesis is coupled with a conformational change in the ATP synthase generated by rotation of the central stalk.[3–5] Despite the success of Boyer's model, and its various extensions based on crystallographic and single– molecule studies developed over the last three decades,[9–13] a comprehensive allosteric pathway elucidating the so called chemomechanical coupling[1,2] between the chemistry of ATP synthesis or hydrolysis and the mechanics of F_1 or V_1 motor action has remained hitherto elusive. In particular, none of the three binding sites, namely empty, bound and tightly–bound sites, involved in ATP synthesis or hydrolysis are directly involved in mechanical–force generation, since these processes occur at subunit–subunit interfaces in the $\alpha_3\beta_3$ or A_3B_3 ring, distant from the stalk within the central pore, where the mechanical force is actually being applied. Consequently, how the chemical energy stored in the ring is transferred to power stalk rotation remains to be addressed.

In the past decade, mechanical energy transfer in ATP synthases has been the object of a host of theoretical investigations, addressing primarily the rotatory motion of F_1–ATPase, the catalytic domain of F_oF_1–ATPase. In many instances, these investigations resorted to a coarse-grained description of the ring formed by the three $\alpha\beta$–subunits arranged in alternation around the coiled– coil stalk, or γ–subunit — a simplification justified by the complexity of the molecular objects at play and the intricate movements involved in the catalytic cycles.[14] Under certain circumstances, the model was simplified even further to a mere elastic network model, yet a sufficiently robust model to capture the physics of energy transduction in the synthesis and hydrolysis of ATP.[15,16]

While general trends eminently relevant to V_oV_1–ATPase have emerged from computational studies of F_oF_1–ATPase, these studies also brought to light a number of controversies, notably on the nature of the torque generated upon ATP–binding, a step underlying rotary catalysis of ATP synthase. Targeted molecular dynamics (TMD) simulations implicated repulsive van der waals interactions between the β–subunits and the stalk as a torque-generating operation.[17] However, it has been argued[14] that the torque observed in TMD reflects more the bias of the simulation than the actual free-energy landscape underlying the coupling of the $\alpha\beta$–subunits with the stalk.[17] In contrast, potential-of-mean-force calculations suggest that the torque results from the electrostatic nature of the stalk–β coupling.[14] This view is consistent with the idea that the motion of the β–subunits constitutes a major driving force for the rotation of the stalk through disruption of the hydrogen– bond network around ATP and the closer packing of the hydrophobic core consecutive to helix movements about the ATP binding site.[18] This view is also compatible with the assumption of a conformational equilibrium of the β–subunit in its empty state being determined in part by electrostatics, notably the mutual interaction of the helices forming the binding site; albeit complete opening of this subunit is enforced sterically by the stalk and arises from favorable electrostatic interactions with the two other β–subunits.[15]

Although atomic force microscopy experiments have cogently demonstrated that ATP–fueled rotary catalysis, however less effective, persists in the absence of the central stalk,[19] the mechanical properties of the latter have been the central focus of a number of theoretical investigations. Rudimentary elastic–network models calibrated from long MD simulations combined with thermal– fluctuation analyses have highlighted a pronounced spatial inhomogeneity in the interaction of the stator with the γ–subunit, resulting in very distinct local elasticity properties.[16,20] While numerical simulations suggest a chronology wherein the conformational transition of β–subunits to their empty state closely follows rotation of the stalk, the rotatory movement of the latter is roughly two orders of magnitude higher compared to experiment.[21] Another stumbling block in the reconciliation of theory and experiment is the ATP–binding dwell, which is observed in single–molecule experiments of F–type ATPases,[22] but presumably absent in their vacuolar form. Numerical simulations have revealed a metastable state, hypothesized to correspond to the ATP–binding dwell identified experimentally. While some authors believe this metastable state to be close to the well– documented structure of F_1–ATPase at 0°rotation,[15] others contend that it is distinct from any known crystallographic structures.[23]

Here, combining transition path sampling[24–26] and free–energy methods,[27–29] we present a comprehensive, detailed model of the ATP hydrolysis–driven rotatory step in V_1–ATPase involving a 120°conformational rotation of the A_3B_3 ring and a physical rotation of the central stalk (DF). The atomic structures required for these simulations are derived from X–ray crystallography of the V_1–ATPase of *Enterococcus hirae*.[1] For the sake of consistent nomenclature the A_3B_3 ring of V_1–ATPase is denoted V_1–ring, and V_1–ATPase is termed V_1–rotor henceforth.

Our study establishes in unprecedented detail the causal relationship between the movements of the AB domains and their role in energy conversion. The results show that the chemical energy arising from ATP hydrolysis is harnessed through the concerted motion of the protein–protein interfaces of the V_1–ring. The interface energy is then transduced into rotation of the central stalk in the V_1–rotor. In fact, even in the absence of a central rotatory stalk, the AB interfaces within the V_1–ring are capable of exchanging energy with ATP hydrolysis. Remarkably, kinetics of chemical to mechanical energy conversion is tuned by the mechanical properties of the ring and the stalk. Altogether, the distinct chronology of events revealed by our study, linking ATP hydrolysis to conformational transitions of the V_1–rotor, resolves on one hand past controversies in ATP synthase bioenergetics, while on the other unifies results from crystallography, single-molecule and mutational experiments.

Simulation design

As illustrated in Figure 1, three different nucleotide–binding sites are identified from the crystal structure: tight (**t**), bound (**b**) and empty (**e**). An empty site (**e**) represents a nucleotide–free state of the binding pocket, which exists either before reactant intake or after product release. A bound site (**b**) is formed after ATP intake into the empty site, but before ATP hydrolysis. Finally, a tight site, (**t**), is achieved when the bound ATP interacts with residue R261 of A–subunit, required to catalyze ATP hydrolysis in the presence of a water molecule. In the following, the ATP hydrolysis–driven rotatory step of V_1–rotor, involving a 120°conformational rotation of the V_1–ring and physical rotation of the central stalk, from prior state R to final state F, as defined in Figure 1d, is described in detail. The difference between a conformational rotation and a physical rotation is that the former indicates a 120°switch in the symmetry of the three aforementioned binding site states without involving any rotational motion, whereas the latter indeed involves a clear motion of the central stalk.

The R → F rotatory reaction is driven by ligand–state changes of the ATP hydrolysis cycle in V_1– rotor. This change is cast in terms of a simple permutation rule: A^eB^e (R) = A^bB^b (F), A^tB^t (R) = A^eB^e (F) and A^bB^b (R) = A^tB^t (F), where A^jB^j (R) [A^jB^j (F)] denotes the ligand–state of the j–th AB interface in state R [state F] of V_1–rotor; $j \in$ (**b**,**e**,**t**).

State R represents a stable state corresponding to the crystal structure. In this state, transition of V_1–rotor to F is not spontaneous. Three subprocesses occurring during the catalytic cycle are required to drive a motor–action phase transition toward F: (**1**) binding of ATP to the empty site, inducing **e** → **b**; (**2**) release of old hydrolysis product (ADP+P_i), promoting **t** →

e; (**3**) formation of a new hydrolysis product through the reaction ATP → ADP+P_i, following **b** → **t**.

Subprocesses (**1**, **2**, **3**) take place somewhere along the R → F transition. Based on prior experimental and computational studies,[7,31–33] subprocess (**2**) is considered rate limiting. Accordingly, we assume in our study that subprocess (**3**) and the diffusion-limited part of (**1**) occur at the very beginning of the R → F transition. To elucidate the rate–limiting nature of subprocess (**2**), we introduce at the AB interface a ligand state **X** = **t** or **t**′, where t′ represents a nucleotide–free state with tight protein conformations. We, therefore, choose to have, respectively, the product released right away (**X** = **t**′), or not released at all (**X** = **t**). The transition modeled is thus R → I → F (Figure 2a), where actually the step I → F is simulated. I corresponds to an intermediate that is energized enough through subprocesses (**1**), (**2**) and (**3**) to drive formation of F. The initial step R → I sets up I but is not simulated. As stated, observation suggests that R → I involves the change in ligand configuration, **e**, **b**, **t** (state R) → **b**$^-$, **b**, **X** (state I). Here, **b**$^-$ denotes an **e** state of loosely bound ATP, in the vicinity of the binding site.

I characterizes a state, in which ATP hydrolysis and new ATP binding in the prior state R have just taken place such that the ATPase is activated to make transition into a new geometry of its subunits, namely the one corresponding to state F. It is constructed from the prior state R as follows: at the A^eB^e interface an incoming ATP molecule is docked in the vicinity of the ATP-binding position (Figure 3, initialization step); exact position and conformation of the ATP molecule is determined from that of an A^b domain when the latter is superimposed to an A^e. This conformation of the A^eB^e interface with ATP, denoted **b**$^-$, implies that the simulation begins at a point where an ATP has diffused into the vicinity of A^eB^e but has not yet bound the pocket via induced fitting as the binding-pocket side-chain conformations still resemble those of an empty site. At the A^tB^t interface, we adopt two alternatives for the ligand state, referring to either state as **X**: in the first case, denoted **X** = **t**′, the hydrolysis product (ADP + P_i) is removed and in the second case, denoted **X** = **t**, we left (ADP + P_i) unchanged in the pocket; position of (ADP + P_i) is determined by superimposing an ADP and Pi onto the ATP position. The other ligand state namely the state **b** at the A^bB^b interface remains unchanged. The resulting system is then simulated for 300 ns and the final snapshot is taken as the intermediate state I.

The modeling of I adopted in the present study relies upon the strategy developed in our previous study of Rho–helicase,[30] and is justified here for the following reasons. First, the timescale for ATP hydrolysis estimated from experiments is shorter than the rate–limiting time for ADP release[34] or P_i release. As R resembles a catalytic dwell structure (the crystal structure was obtained while binding to V_1–rotor a non–hydrolyzable ATP analogue), ATP hydrolysis in R will necessarily precede the conformational transition towards F. Second, for an ATP concentration of 40 mM in *Enterococcus hirae*, the timescale for ATP binding is on the order of 0.5 ms,[33,35] which is much shorter than the timescales of the other two processes combined, i.e., ATP hydrolysis and product release. One ATP molecule will, therefore, very likely diffuse to the e (empty) site of R and become transiently bound in I (**e**→**b**$^-$ at the A^eB^e interface) before the other two ligand processes take place. Thus, whether the product (ADP+P_i) release is indeed crucial to induce A^eB^e–binding of the

incoming ATP and subsequent conformational transition is explored here by I → F simulations assigning for state **X** either state **t** or state **t′**.

However, first, a simplified system is prepared for testing whether the stated R → I → F formulation captures a rotational transition pathway accurately. The conformational rotation of an isolated V_1–ring is chosen for this purpose. Prepared by removing the stalk from the crystal structure of V_1–rotor, the V_1–ring is experimentally known to involve conformational rotation fueled by ATP hydrolysis.[1,19] Thus, simulating the conformational rotation of the V_1–ring is expected to provide valuable insights into the role of conformational transitions at the AB interface before introducing further complications arising from changes in the ring–stalk interactions in the complete V_1–rotor. In Figure 2b, the superscript* is used to designate stalk–free structures involved in designing the simulations for V_1–ring conformational changes. The stalk is then reintroduced into structures from the V_1–ring transition path from I^* to F^*, to ultimately obtain the I → F transition path accompanying ATP hydrolysis within V_1–rotor.

As detailed in the Methods section, the ATP–hydrolysis–driven 120°conformational rotation of the V_1–ring and physical rotation of the central stalk in V_1–rotor is structurally resolved at the atomic level employing a combination of transition path search and optimization approaches including anisotropic network modeling (ANM),[36] targeted molecular dynamics (TMD),[25] and the so–called string method.[26,37] Free–energy changes are measured for both the V_1–ring ($I^* \rightarrow F^*$) and rotor (I → F) conformational transition pathways employing bias–exchange umbrella sampling (BEUS) computations to measure the changes in mechanical energy during rotatory step.[38–40] To relate the chemical and the mechanical energy involved in the rotatory step of V_1–rotor, binding affinities of the nucleotides in the ATP-binding pockets are determined employing alchemical free-energy calculations;[27] ratio of the changes in chemical and mechanical energy changes during a rotatory step indicates the energy-efficiency of the motor. Finally, rate measurements are performed with maximum–likelihood methods[28] as a route to access the turnover of ATP hydrolysis for direct comparison with single–molecule measurements of V_1–rotor.

Results

In what follows, first, employing FEP[41,42] methods nucleotide (ATP or ADP+P_i) binding affinities of the A–domain are computed for the empty (**e**), bound (**b**) and tight (**t**) sites in the prior state R^*, and for the loosely–bound $\mathbf{b}^-$, bound (**b**) and **t′** sites in intermediate state I^* of the V_1–ring. The difference in the nucleotide binding affinities between states R^* and I^* measures up to the nucleotide–binding induced energy change that chemically activates the V_1–ring from the low–energy prior to the high–energy intermediate. This high–energy intermediate state is then allowed to relax to a ground state, F^*, via a string simulation, which captures the ATP hydrolysis–driven conformational rotation pathway of the V_1–ring. **Detailed in Refs**.[26,37] string method is a path-finding algorithm that can be used to locate an approximate minimum free energy path between two free energy minima in a high-dimensional space of atomic coordinates or collective variables. Next, the string simulation is repeated with the central stalk (DF) introduced into the V_1–ring; this simulation captures the 120°rotation of the stalk within the entire V_1–rotor between states I and F. The $I^* \rightarrow F^*$

and I → F transitions are analyzed further to probe the mechanical properties of the ring and the central stalk, identify key mutations, and determine an allosteric regulation scheme that underlies the millisecond–scale energy storage and transduction of the V_1–rotor. Free–energy and rate estimations along the $I^* \rightarrow F^*$ and I → F transition pathways, derived employing BEUS and maximum–likelihood procedures, respectively, demonstrate the thermodynamic feasibility of these pathways, locate reaction intermediates and kinetic bottlenecks, and quantifies the chemomechanical energy conversion efficiency of the V_1–rotor. A schematic summarizing the key findings of the present work is provided in Figure S1. It showcases the logical order upon which the results are organized, and further allows easy navigation through the following subsections.

Chemical activation of V_1–ring follows from ATP hydrolysis

The standard binding free-energies for the different binding sites of the nucleotides, either ATP or ADP + P_i, are gathered in Table 1. They indicate that ADP + P_i association to the A domain is energetically less favorable by about 3 kcal/mol than that of ATP in the tight (**t**) site, and by about 1 kcal/mol than that of ATP in the bound (**b**) site. Not unexpectedly, binding affinities of both the nucleotides in the empty site (**e**) are nearly identical and appreciably lower than in either the **t** or the **b** sites. It is worth noting that this binding-affinity trend mirrors that of F_1–ATPase, as also reported in Table 1.[43,44] The trend is also in fair agreement with recent binding-affinity measurements of ATP and ADP + P_i in their respective t and e states by Adachi et al.[REF]

Notwithstanding this qualitative agreement, we find an apparent discrepancy between V_1–ATPase and F_1–ATPase for the binding of the hydrolysis product, ADP + P_i to the **t** site of the V_1- or F_1-ring. Specifically, the binding affinity appears to be about 2 kcal/mol weaker in F_1–ATPase, where association of ADP + P_i to the α domain corresponds to approximately the same free energy in the **t** and **e** sites. These discrepant results are consistent with the commonly accepted view that ADP inhibition of V–type ATPases slows down product release, and renders them less efficient than their F-type homologues.

The free–energy difference between the **t** and the **e** sites for ATP amounts to about 7.5 kcal/mol in V_1–ATPase and about 7.2 kcal/mol in F_1–ATPase. This difference represents the chemical free energy gained by the V_1–ring from losing a hydrolysis product at the **t** site (creating a $\mathbf{t}'$ site) and concomitant loose-binding of a new reactant ATP at the **e** site (creating a $\mathbf{b}^-$ site), which activates the state $R^* \rightarrow I^*$. Following energy conservation, therefore, approximately 7.5 kcal/mol of energy is made available to I^* for subsequent mechanical transduction.[3,44] In the following sections, the mechanical transduction will be decomposed into two distinct contributions, namely the conformational rotation of the V_1–ring, and the rotation of the stalk in the whole V_1–rotor.

Conformational rotation of V_1–ring is thermodynamically favorable

Single–molecule experiments reveal that an isolated V_1–ring, i.e., a V_1–rotor bereft of the DF stalk, exhibits enzymatic activity.[1,19] Under these premises, we chose to investigate the conformational rotation of the isolated ring and subsequently, in the next section, introduce the stalk to assess the effect of the latter on the chemomechanical coupling efficiency of the

V_1–rotor. Investigation of V_1–rotor requires that a causality relationship between the V_1–ring and stalk dynamics be established. In other words, we will address what are the AB protein interfaces at play and identify the chronology of their interaction to manifest ultimately rotation of the central stalk.

Conformational rotation pathway of V_1–ring—String simulations with swarms of trajectories[26] illuminate the milestones that follow ATP hydrolysis in the V_1–ring, namely states I^* through F^* in Figure 3. It ought to be reminded that since product release cannot be modeled in these simulations, two distinct transition pathways were investigated, one with ADP+P_i present in the tight site (**t**), and one devoid of it (**t′**). Even though a t site has not yet been crystallographically determined within the V_1–ring, feasibility of such a site is confirmed by a combination of biochemical and single–molecule experiments. These investigations depict significant ATP hydrolysis in both V_1 and F_1-rings [REF], reaffirming the presence of the t site where residue E261 interacts with ATP to cleave the terminal phosphate [REF]. Described as follows, both the t and t′ pathways correspond to the same sequence of events (see Figure 3).

First, $A^{t*}B^{t*}$ becomes $A^{e*}B^{e*}$; concomitantly, the $\mathbf{b}^-$ site with the loosely-bound ATP in an adjacent $A^{e*}B^{e*}$ interface further opens allosterically into a site germane to ATP binding, which, henceforth, will be referred to as bindable site (**bi**). The **bi** site is enclosed within an $A^{e*}B^{e*\prime}$ interface, where $B^{e*\prime}$ provides a more open conformation than B^{e*}, facilitating access of the loosely–bound ATP to the ATP–binding residues (Table S3 in supporting information). Taken together, in the first step the state I^* (**b**$^-$,**t′**,**b**) is transformed to state II (**bi**,**e**,**b**). In the second step, ATP associates to the **bi** site on A, transforming $A^{e*}B^{e*\prime}$ into $A^{b*}B^{b*}$. At this stage, two sites of the V_1–ring are occupied by ATP in the bound (**b**) conformation, characterizing state III (**b**,**e**,**b**). Finally, the third site, previously in a bound conformation, i.e., in the absence of the incoming ATP, undergoes now an $A^{b*}B^{b*}$ to an $A^{t*}B^{t*}$ conformational transition yielding the F^* (**b**,**e**,**t**) state.

Altogether, we find that the $R^* \rightarrow F^*$ transition follows the chronology: R^* (**e**,**t**,**b**) → I^* (**b**$^-$,**t′**,**b**) → II (**bi**,**e**,**b**) → III (**b**,**e**,**b**) → F^* (**b**,**e**,**t**). Details on allosteric interactions between groups of residues that underly the $I^* \rightarrow F^*$ segment of the $R^* \rightarrow F^*$ transition pathway are provided later in the Results section.

Determination of the free–energy change along the optimized, most likely pathway allows the different conformational states to be hierarchized. We find that states II (**bi,e,b**) and III (**b,e,b**) of Figure 4 are metastabilities, or local minima of the free–energy profile, and, therefore, constitute potential intermediates in the catalytic cycle. Presented in Figure S11, these states strikingly resemble crystallographic structures of the V_1–ring,[1] i.e., state II possesses a distance RMSD with respect to PDB structure 3VR2 of 2.2 Å, while state III is 2.5 Å apart from PDB structure 3VR3. The free–energy difference between state I^* and state F^*, which embodies the endpoint of the 120°–conformational rotation, is in the order of $k_B T$ at room temperature, indicative that the overall process is slightly thermodynamically favorable. This conclusion is supported by single– molecule studies in F_1–ATPase, where the isolated $\alpha_3\beta_3$ ring is indeed shown to operate in the direction of ATP hydrolysis, but sometimes also in an opposite direction indicating the lack of a substantial thermodynamic

drive for conformational rotation of the ring.[19] The main barrier of the one-dimensional free–energy profile, that is the rate-limiting step of hydrolysis after product release and in the absence of the stalk, arises between states II and III, amounts to about 2.3 kcal/mol. This barrier reflects the free–energy cost towards the binding of ATP in the empty state, which requires isomerization of the gatekeeper residue $R350^1$ of domain B^{e*} to facilitate entry of the nucleotide into the binding pocket and its subsequent stabilizing interaction with residues G235, G237, K238 and R262 (see Figure S10) pertaining to the A domain.

Mechanical properties of the V_1–ring—To investigate the mechanical properties of the V_1– ring, we resort to a dynamic network analysis of the string trajectory, which highlights correlated subdomains of the enzyme and help identify allosteric pathways connecting the movements of these subdomains [REF]. As illustrated in Figure 6, the network analysis partitions each of the A and B domains into three subdomains, making a total of 18 subdomains for the entire V_1–ring. Remarkably enough, the nucleotide binding pocket lies at the confluence between two of the three correlated subdomains that form an A domain. The spatial arrangement of these two subdomains is suggestive of a hinge–bending–like motion upon nucleotide binding,[18,45] as confirmed by the measurement of the bending angle defined in reference 45. The variation of the bending angle amounts to about 20°for the transition between A^t to A^e, to about 15°for the transition between A^b to A^e and about 5°for the transition between A^t to A^b (see the chronology depicted in Figure 9 and Figure 10, illustrating different extents of hinge–bending within the computationally derived intermediates, also presented in Figure S15 and Figure S12).

Nucleotide binding is anticipated to induce conformational transition in the binding site of the A domain (see Figures 3, 5 and S15), further promoting the hinge–bending motion between the correlated subdomains, which, in turn, is expected to have bearing on the movement of the stalk in the full V_1–rotor. In the docking of the nucleotide onto the A domain, residue F425 is identified as a key actor — in analogy with F424 in F_1–ATPase,[9] forming a stabilizing π–π stacking with the adenine base, while also contributing to the moving subdomain that is envisioned to interact with the DF stalk.

Stalk rotation of V_1–rotor harnesses energy from ATP hydrolysis

So far, we have seen that notwithstanding the absence of the central stalk, V_1–ring is capable of enzymatic activity (Figures 3 and 4).[1,19] We will now show in light of independent simulations, that the efficiency of ATP hydrolysis can be appreciably enhanced by dint of the DF subunit.

Stalk rotation pathway—Qualitative examination of the simulations performed employing the string method with swarms of trajectories of the entire V_1–rotor did not reveal any significant difference in the conformation of the V_1–ring, relative to the simulations bereft of the central stalk, as mirrored in Table S3. Analysis of the sequence of events characterizing conformational rotation of the ring in concert with the stalk rotation within the V_1–rotor, however, brought to light an additional, subtle, albeit key milestone, namely a second (**b,e,b**) state that was missing in the $I^* \rightarrow F^*$ pathway for the V_1–ring transition (see Figures 5 and 3).

Similar to the ring transition outlined above, first, A^tB^t transforms into A^eB^e, which prefaces further opening of the adjacent A^eB^einterface, transforming a $\mathbf{b}^-$ site into a bindable (**bi**) site. The bi site is enclosed within an $A^{e'}B^{e'}$ interface, where $A^{e'}$ and $B^{e'}$ provide more open conformations than A^e and B^e, respectively, facilitating access of the loosely–bound ATP to the ATP–binding residues (s). Taken together, in the first step, state I ($\mathbf{b}^-$,$\mathbf{t}'$,**b**) transitions into state 1 (**bi,e,b**). The stated $A^tB^t \rightarrow A^eB^e$ transformation during the I → 2 transition also weakens the AB–stalk interface, allowing the bent stalk to straighten out (see movie M5 in the Supporting Information). Second, upon ATP association to the **bi** site of the A domain, the corresponding $A^{e'}B^{e'}$ interface closes through a hinge-bending motion to A^bB^b i.e. the binding site undergoes a **bi** → **b** transition (see Figures 7a and s); this transition yields the first doubly-bound state, denoted 3 ($\mathbf{b}'$,**e**,**b**), prior to the rotation of the stalk. The AB interface enclosing the $\mathbf{b}'$, site is denoted $A^{b'}B^{b'}$ henceforth. Note, this additional ′-notation introduced for denoting the first A^bB^b interface is meant to only distinguish between the two A^bB^b interfaces captured by the I → F transition, and unlike $A^{e'}B^{e'}$ above, does not indicate any new AB conformation. $A^{b'}$ and A^b, in fact, capture identical conformations of the A domain, which differ by an RMSD of < 1 Å; the same holds for $B^{b'}$ and B^b. Thus, in the second step, a transition from 2 → 3 is accomplished via the so called $A^{e'}B^{e'} \rightarrow A^{b'}B^{b'}$ transformation. This transformation induces a wring deformation on the straightened central stalk at the locus where it interacts with the newly formed $A^{b'}$ domain. Third, the wrung stalk rotates by 120°, leading to the aforementioned second (**b,e,b**) state, denoted 4. Last, the bound site (**b**) already occupied by ATP evolves into **t** completing the transition to state F (**b**,**e**,**t**). The $A^bB^b \rightarrow A^tB^t$ transformation during the 4 → F transition induces a bend on the 120°-rotated stalk, reestablishing its adhesive interface with the newly formed A^tB^t. Altogether, we find that the R → F transition follows the chronology: R (**e**,**t**,**b**) → I ($\mathbf{b}^-$,$\mathbf{t}'$,**b**) → 2 (**bi,e,b**) → 3 ($\mathbf{b}'$,**e**,**b**) →stalk-rotation→ 4 (**b,e,b**) → F (**b**,**e**,**t**).

A second notable observation is that, at any point across the pathway, the nucleotide (ATP or ADP + P_i) binding affinity of the binding pocket in the A domain is correlated with the A-stalk interaction: the **e**, **b** and **t** sites with the lowest, intermediate and highest ATP-binding affinity respectively belong to A^e, A^b and A^t domains that characterizes minimal, primarily electrostatic, and combined electrostatic and hydrophobic interactions with the stalk (Table 1, and Figures 9, S15 and Figure 10).

The free–energy profile that underlies stalk rotation is depicted in Figure 4. In stark contrast with that representative of the isolated V_1–ring, the free–energy change between the end states now amounts to about 6 kcal/mol. Noteworthily, this quantity is in close agreement with the theoretical value obtained for the F_1–ATPase analogue.[14] Moreover, it is commensurate with the nucleotide binding/unbinding–induced chemical work determined above from free–energy perturbation calculations (Table 1) and shown in the thermodynamic cycle of Figure 7b, implying thereby identification of an efficient chemomechanical coupling pathway that converts a significant amount of the chemical energy from ATP hydrolysis into the conformational changes of V_1–rotor. Just like in the absence of the DF subunit, states 2 (**bi,e,b**), 3 ($\mathbf{b}'$,**e**,**b**) and 4 (**b,e,b**) of Figure 4 are local minima of the one-dimensional free–energy profile. States 2 and 3, on the one hand, and states 3 and 4, on the

other hand, are separated by appreciable free–energy barriers, about 3.5 and 4.5 kcal/mol, respectively. In the course of the first conformational transition, i.e., state 2 to 3, hydrophobic residues L28 and L155 of the central stalk become marginally exposed to water (Figures 5 (upper-inset) and S19), resulting in an increase of the free energy; the binding of ATP to the **bi** site accompanying this 2 → 3 transition, which was observed before during the state II → III transition of the V_1–ring conformational rotation pathway (Figure 3(inset)), also contributes to the 3.5 kcal/mol barrier. During the second conformational transition, i.e., state 3 to 4, salt bridges between residues E161, R164 and R165 of the stalk and E472 and R475 of the $A^{b'}$ domain and E384 and $B^{b'}$ domains are being reorganized, involving transient repulsive electrostatic interactions of residues E161 (DF) and E472 ($A^{b'}$), on the one hand, and residues R164 (DF) and R475 ($A^{b'}$), on the other hand, which cause the free energy to rise (Figure 5(lower-inset)). Once the new salt bridges are established, a net free–energy decrease by about 1.5 kcal/mol is measured.

The free–energy calculations reported here can also be utilized as a basis for kinetic modeling (see Methods and supporting information). The transition rates associated to the different milestones in a 120 °–rotation step of the full catalytic cycle are gathered in Figure 5. Noting that the mean first passage time of 1.09 ms (Figures 5 and S9c) estimated for the 120°rotation should be corrected by the diffusive ATP entry or product–release time, which was evaluated in an independent investigation of ATPases to be approximately 2.6 ms,[33] one complete 360°rotation is expected to take 3 × (2.6 + 1.09) = 8.07 ms. These rate estimates add up to about rotation speed of 92.5 s^{-1}, which is in good agreement with the experimental measurement of a maximum rotation speed of 107 s^{-1}.[7] Furthermore, in sharp contrast with F_1–ATPase,[46] and in strong agreement with single-molecule experiments on V_1–ATPase,[31] we did not observe any dwell phase during stalk rotation.

An alternate transition pathway examined herein involves the same conformational rotation of the V_1–ring and stalk rotation, but ignores product release, as illustrated in Figure 2, that is when **X** = **t**. As can be seen in Figure S13, the considerable free–energy barrier, in excess of 11 kcal/mol, suggests that this pathway is unphysical and that product release should precede ATP binding to the empty site and subsequent conformational transition inducing stalk rotation. If the product remains in the binding pocket, then the $A^t \rightarrow A^e$ transition is hindered and volume of the central pore allows rotation only if the stalk sterically interacts with the transformed A^e raising thereby the energy of the system. The underlying one–dimensional free–energy profile features an early intermediate, which corresponds to a straight stalk, yet with the V_1–ring conformation resembling that of the A^tB^t state.[47]

Finally, models from states 1–4 were subjected to alanine scanning on the Robetta server.[48] As noted in Table S4, majority of the residues identified for stabilizing the domain A–DF stalk and domain B–DF stalk interfaces are in perfect agreement with mutational studies of the V_1-rotor; Described below, several of these residues play a key role in driving allosteric interactions between the V_1–ring and the central stalk to enable the chemomechanical coupling. In addition, we predict residues V300, R303, R333, E352 of the A domain and R221 of the B domain are responsible for stabilizing the AB interface, even in the absence of the binding nucleotide; this prediction can be tested via future experiments.

Mechanical properties of the stalk—The torsional elasticity of the central stalk was inferred from the angular fluctuation in the course of a 300–ns unbiased simulation at thermodynamic equilibrium, using the definition of reference 20. Projection of the elasticity onto the DF subunit is depicted in Figure 8, and reveals acute spatial inhomogeneity, with the central region exhibiting maximal rigidity, whilst the termini are significantly more flexible. This inhomogeneity can be partitioned spatially into five strata, i.e., L1 through L5, representing portions of the stalk endowed with distinct torsional elasticities. Not unexpectedly, the elasticity modulus of the stalk increases in the presence of the V_1–ring, as mirrored in Figure 8. The present findings are in line with the spatial decomposition proposed for the γ–subunit,[16,20] and domain complaince of the F_1– ATPase.[REF]

The new picture of the central stalk of V_1–rotor portrayed by the present set of simulations is not that of a rigid body. In the course of the catalytic cycle, the DF subunit chronologically straightens (state I → 2), locally wrings (2 → 3), rotates (3 → 4) and bends (4 → F) (see movie in the Supporting Information). Surprisingly, it is observed that the most rigid layer of the stalk both in the presence versus absence of the V_1–ring, namely L3, has the least direct interaction with the ring inside an entire V_1–rotor. This result implies that the stalk is inherently designed to be flexible only in regions where it interacts with the ring. Such inhomogeneous distribution of flexibility has energetic consequences, as stated in the following.

Comparison of the one-dimensional potentials of mean force in the presence of and without the central stalk (see Figure 4) reveals that the stalk lifts the V_1–ring conformational–state degeneracy. Physically speaking, the (**b,e,b**) state of the ring suffices to hold the elastic stalk in two distinct conformations — the first one is straight and locally wrung, while the second one is rotated. It ought to be clearly understood that removal of conformational–state degeneracy is only possible owing to the elastic nature of the stalk, which permits local deformations necessary for stabilizing V_1–rotor in state 3 prior to rotation towards state 4 (see Figure 5). Were the DF subunit rigid, the free–energy barriers against rotation would add up to at least about 3.5 + 4.5 kcal/mol, that is 8.0 kcal/mol, which translates to a transition rate nearly two orders of magnitude slower than predicted above. Flexibility of the central stalk, therefore, represents a remarkable design principle that benefits the catalytic efficiency of ATP hydrolysis in V_1–rotor in addition to the chemomechanical energy conversion efficiency already reported above.

Ring-stalk allosteric interaction in V_1–rotor

At this point, on the basis of μs–simulations addressing ms–timescale biological processes, we have painted a quantitative picture of the chemomechanical coupling in V_1–ATPase, and, wherever possible, verified our novel findings with available experimental and theoretical insights. We will now examine, for the very first time for V–type ATPases, the synergy between the dynamics of the nucleotide binding pocket, the hinge–bending motion in the A domains of the ring and the rotation of the central stalk to elucidate an intricate causality relationship underlying ATP turnover (see movie in the Supporting Information).

State I to state 2 transition—In the course of the transition between state I and state 2, in the absence of ATP in the tightly bound pocket, residue F425 is essentially exposed to the aqueous environment, which corresponds to an enthalpically unfavorable state. To remedy this situation, the phenyl ring is displaced towards a neighboring cavity lined with hydrophobic residues V240 and F506. This displacement of the side chain is allosterically coupled to the hinge–bending motion undergone by A^t, as shown in Figure 6. Consequently, the A^t subunit swivels outwards by about 20 °, transitioning into A^e, and the stalk has straightened up (Figure 9). As the latter occurs, non– polar residues L28 and L155 borne by the stalk have sought shelter in the adjacent $B^{e'}$ subunit of the $\mathbf{b}^-$ site, reorganizing hydrophobic packing. Concomitantly, the salt bridge established between residues R24 of the stalk and E472 of A^t is disrupted and replaced by the interaction of R24 with E396 of the newly formed A^e. Substitution of both hydrophobic and electrostatic interactions is crucial to optimize the free–energy cost incurred during the transition from state I to state 2. As noted by Arai et al,[1] in the absence of a bound nucleotide, the A^t subunit is expected to interconvert spontaneously to A^e — a step consistent with the witnessed decrease in free energy (see Figure 4).

The A^t domain is joined with the B^e from the $\mathbf{b}^-$ site via hydrophobic interactions between I473 of the former and V387 of the latter (see Figure S14). Guided by this hydrophobic contact, the outward swivel of A^t induces allosterically a similar movement of B^e domain, opening up therefore the A^eB^e interface into a bindable $A^{e'}B^{e'}$ to allow ATP binding (Figure 5).

State 2 to state 3 transition—To a certain extent, this transition from $A^{e'}B^{e'}$ to $A^{b'}B^{b'}$ can be viewed as the inverse of that from A^tB^t to A^eB^e, i.e., state I to state 2. As ATP crawls into the bindable site, key–residue F425 forms a π–π stacking interaction with the adenine base, which is accompanied by an inward swiveling motion of the $A^{e'}$ subunit by about 15°. At the same time, $B^{e'}$ undergoes a conformational transition to $B^{b'}$, sliding over $A^{b'}$, in order to maximize contact with the bound nucleotide. The space liberated at the central pore of the ring from this sliding transition at the $A^{b'}B^{b'}$ interface is conducive to a structural deformation of the stalk. Indeed, a local wringing deformation of the stalk follows at the point of contact with the newly formed $A^{b'}$ and A^e, which is a necessary step to prevent water exposure of residues L28 and L155 on the stalk— see Figures 5 (upper-inset) and S19. Concurrently, the salt bridges between residues R14, R24, D34 and R38 of the stalk and residues E352 and E396 of A^e, and R475 and E472 of $A^{b'}$ are ruptured, resulting in the solvation of the titratable side chains (see Figure S15 and Figure S19), consistent with the positive net free–energy change of Figure 4. This increase in free energy remains moderate by virtue of aforementioned stalk residues D34 and R38 encountering new partners in the A^e domain, and R14 in the B^e domain: D34 and R38 respectively reconnects with R475 and E472 of the transformed A^e, while R14 strengthens interactions with D310 of the transformed B^e. (see Figure S16 and movies M1 to M5). The dangling E396 of A^e, left after the wringe-induced rupture of its interactions with R24, now transiently interacts with R17 from the stalk. Similarly, the dangling E472 of $A^{b'}$ starts interacting with another residue from the stalk, namely R164 (see movie M2).

State 3 to state 4 transition—The wringing deformation of the DF stalk incurred over the state 2 → state 3 transition disrupts several key stalk–V_1–ring interactions across all the 5 strata of the stalk (Figure 8). Though, lost interactions of a few residues, such as the aforementioned D34 and R38 of layer L5, are resurrected at the stalk–A^e interface, and R14 is transiently bound to D310 of the transformed B^e, electrostatic interactions of most other residues including R194 from L1, E180 from L2, R24 at the boundary of L3 and L4, and E161, R164, R165 from L4 remain either completely or partially unsatisfied after the wringing deformation. Rotation of the central stalk follows to reinstate the lost interactions of these residues. Presented in Figure S18, first, the R194 from L1 binds to E347 from A^e following which E180 and R14 from L2 combines with R271 of $B^b$and E352 of A^b and thereafter residues E161, R164 and R165 from layer L4 reorganizes to be stabilized by R475 of the $A^{b'}$, E384 of $B^{b'}$ and E472 of $A^{b'}$ respectively.

Summarizing the order of re-organizing interactions described across the state 2 → state 3 and state 3 → state 4 transitions, the rotation of the central stalk is perceived as a coordinated movement of its individual layers. Deformation of layer L5 (via rearrangement of residue L28 and L155) and L4 (via rearrangement of residue D34 and R38) due to swiveling in of the A-subunit ($A^{e'} \rightarrow A^{b'}$) induces subsequently rotation of layers L2 (via rearrangement of residue R14) and L1 (via rearrangement of residue E180). L3 being the least ring-interacting part of the stalk rotates adiabatically in response to the L2 rotation. The layer L4, fraught with the highest thermodynamic barrier rotates last. In fact, the thermodynamic drive provided by the rotation of all the other layers of the stalk, namely L1-L3 and L5, cooperatively alleviates the rotational barrier of L4, permitting an overall millisecond–timescale rotation.

It is worth noting that the AB binding interfaces are only minimally affected during the stalk– rotation step, i.e. state 3 to state 4 transition. This result implies that reorganization of the V_1–ring and rotation of the stalk are not entirely concerted in V_1–rotor. There is a rate–determining kinetic lag on the order of 1 ms (Figure 5), which is utilized between states 3 and 4 for the storage of elastic energy prior to its transduction across the stalk to induce rotation. The partially concerted V_1–ring rearrangement and stalk rotation, which diminishes the rate of ATP hydrolysis is expected to be a part of the overall design of the V_1-rotor, considering that it contributes about 50–75% of the catalytic efficiency of an entire V_oV_1–ATPase.[1] Presence of the V_o domain is envisioned to modulate the mechanical property of the stalk to overcome the partially concerted structural changes in the V_1-rotor, thereby enhancing the overall catalytic efficiency of the entire V_oV_1– motor.[35] In fact, the lack of any rotational substeps in V_1–ATPase is also a direct result of these disconcerted motions. On the contrary, past studies have shown that F_1–ATPase has clear 80°-40°substep features, where the last 40°rotation is strongly concerted with the ring conformational changes [REF].

State 4 to state F transition—The final step, namely the transition between state 4 and state F, involves deeper penetration of a bound ATP into its binding pocket, thus enabling the interaction of the terminal phosphate with the E261 residue. This interaction is key to initiate ATP hydrolysis.[1,49] Concomitant with the deeper entry of ATP, the A domain swivels further in by 5°, transforming A^b into A^t (Figure10). The R24–E472 salt bridge that was replaced in the transition between state I and state 2 by the R24–E396 interaction, subsequently lost in

the transition between state 2 and state 3, as the ancillary R17–E396 interaction forms transiently, is now recovered through the interactions of R24 of the 120°–rotated stalk with E472 of the transformed A^t. Recovery of this interaction causes the stalk to bend towards the A^tB^t interface, thus completing the transition. Combined with the aforementioned three transitions, this last step completes the detailed picture of the conformational rotation of the V_1–ring in conjunction with the physical rotation of the stalk.

Energy storage and transduction

The current simulations provide direct insight on the mechanism of energy storage and transduction within V_1–rotor. We observe that the chemical energy from ATP hydrolysis is stored as difference in binding affinity between the **e**, **b** and **t** binding sites of the V_1–ring (Table1), measuring up to 7.5 kcal/mol. This energy is harnessed by the AB and AB-stalk interfaces of the V_1–rotor for a period of 1.09 ms (Figure 5) during which, the swivel–in or out of the A–subunit (States I → 2, and 2 → 3 transition) and sliding of the B-subnit over A (2 → 3 transition) induce the 120°rotation of the stalk (3 → 4 transition); energy cost of these transitions sum up to 6 kcal/mol (Figure 4). Therefore, the overall chemomechanical energy conversion efficiency of the V_1–rotor is estimated to be (6 kcal/mol)/(7.5 kcal/mol) × 100 = 80%.

The AB interfaces within an isolated V_1–ring utilize at least 0.6-2 kcal/mol of chemical energy during the I^* to F^* transition, when the stalk is absent (Figure 4). Introduction of the stalk enhances the amount of energy harnessed within these AB interfaces to 4 kcal/mol (Figure S20), as measured from the free energy difference between states I and F employing only 1,179 collective variables from the six AB interfaces. This enhancement stems from the fact that AB interfaces in the V_1–rotor is stronger than those in the isolated V_1–ring: stalk-AB interactions stabilize the bound nucleotide conformations within the A domain (reported above along with the stake rotation pathway and in reference 1), also maximizing interactions of the nucleotide with the B domain to provide altogether a stronger AB interface in the V_1–rotor than in the isolated V_1–ring. Altogether, conformational transitions of the AB interfaces in V_1–rotor takes up about (4 kcal/mol)/(6 kcal/mol) × 100 = 66% of the total mechanical energy harnessed during the I → F transition. Thus, our results suggest that the majority of V_1–rotor action is driven by transitions of the AB interfaces, while the stalk rotation follows spontaneously.

Discussion

The present study provides an all–atom picture of the ATP hydrolysis–driven conformational and stalk rotation dynamics within the V_1-rotor of a V_oV_1–ATPase. Notwithstanding the atomistic simulations performed in recent years primarily on the ring proteins of the F–homologue,[15,16,18,20,34,45,49–51] alongside coarse–grained simulations carried out on the entire F_1 rotor,[14] to the best of our knowledge, the present work provides the only example to date that addresses simultaneously the chemical detail of the problem at hand, together with the millisecond timescale of the entire 120°transition. We observe, in qualitative agreement with the hypothesis put forth from crystallographic studies, that product, i.e., ADP + P_i, release is closely followed by ATP binding, which, in turn, induces sliding of the

AB interface to achieve rotation of the central stalk. All–atom simulation of the V_1–rotor was, however, necessary, as we have now established that (**i**) the energy required for the rotation of the stalk is harnessed within the AB interfaces of the V_1–ring, mediated by ATP or ADP + P_i binding at these interfaces, and (**ii**) the mechanical properties of the stalk are perfectly tuned to optimize the kinetic barriers of rotation and, hence, enable the millisecond rotation timescale. Flexibility of the central stalk chiefly allows it to sustain two distinct conformations within a similarly configured V_1–ring, thereby lowering the kinetic barrier for rotation, which would have been nearly two orders of magnitude higher, were the stalk completely rigid. We further note that even though the overall free–energy change in V_1–rotor is very similar to that in F_1-rotor, differences in the binding affinity of the product with the post–reaction site (namely **t** for V_1–rotor versus **DB** for F_1-rotor) is higher for **t**, thus, making ADP inhibition more rate–limiting for the former.

Our simulations, however, fail to capture the reactant, i.e., ATP, binding or product, i.e., ADP+P_i, release events, owing to limitations of the string algorithm to sample the orthogonal space. Free–energy barriers are particularly high for the product–release step due to strong electrostatic interactions between the phosphate groups and the K238, R262 and R350 residues in the nucleotide–binding site (Figure S10),[7] as also demonstrated above in the free–energy perturbation calculations, thereby limiting further the applicability of the string method to capture ADP+P_i release. The rate–determining contribution of these events is in fact accounted for by factoring in either the ATP binding or the ADP+P_i unbinding rates from independent experimental and computational studies.[32,52] Here, we note that the product–release rate of 43 ms[33] is much slower than those for the different conformational transitions. Nevertheless, at saturating substrate concentrations, when the kinetic barriers for binding are not rate–determining, the conformational transitions involving the rotational power–stroke is rate–determining, as has been well established for F–type ATPases.[51]

The present work also illuminates that the ATP binding step does not constitute the only criterion for torque generation. Binding of ATP is limited to the A subunit and induces an inward hinge– bending motion of the A^e subunit, which, in turn, allows A to interact with the stalk. Stalk rotation is, however, only possible as the B-subunit slides over A, to maximize its contact with ATP. This sliding motion liberates space within the central pore of the V_1–rotor for the stalk to deform and subsequently rotate. It is, therefore, the movement of the AB interface that guides that of the stalk. We hypothesize this interface movement-driven stalk rotation to be a more general feature of V– as well as F–type ATPases. The hypothesis gains steam from observations whereby specific ring–stalk interactions are found to play a minor role toward the torque generation.[53]

The simulations reported herein further bring to light a network of allosteric interactions regulating the cross–talk between the motion of the AB domains of the ring and that of the DF stalk. The majority of these interactions is electrostatic in nature, with their reorganization posited to be rate–limiting. However, to achieve one distinct milestone along the pathway, hydrophobic interactions also play a key role. In particular, hydrophobic residues induce a wringing deformation, which precedes the electrostatically driven rotation. Throughout this process, water plays a major role at the ring–stalk interface (Figure S19), reducing the barriers of side–chain dissociation and association that drive stalk rotation.

Noteworthily, about 80% of the energy liberated during ATP hydrolysis is utilized by the conformational transition.

Put together, the overall picture painted in the present investigation provides a unified view on the chemomechanical coupling that underlies the catalytic cycle of V_1–rotor, reconciling seemingly discrepant standpoints. In particular, the molecular mechanism of conformational and stalk rotation inferred from our simulations agrees well with the conclusions drawn by Mukherjee and Warshel of a rotary–chemical coupling primarily driven by electrostatic interactions, which also include the effect of the ionic charge solvation on hydrophobic and polar residues.[14] This idea, however, does not necessarily contradict that of Pu and Karplus of a rotary movement of the stalk imparted by van der Waals repulsive forces, notwithstanding the local nature of the latter.[17] It simply ought to be expanded by invoking the mechanism of hydrophobic hydration proposed herein, central to the ring–stalk allosteric regulation, which imposes an enthalpic barrier surmounted by side–chain displacement coupled to a hinge–bending motion of the A subunit propagating to the stalk. Furthermore, as had been anticipated by Gao et al., differences in the binding affinities account for the conformational–transition energetics in the V_1 –ring.[44] Consistent with the work of Czub and Grubmüller,[15] our simulations of V_1–ring appear to refute the earlier hypothesis of a push–pull mechanism for the DF subunit.[54,55] They also reveal, in line with experiment,[1] that in the absence of the DF subunit, the V_1–ring is looser, relative to the full V_1–rotor, as evidenced by the available crystallographic structures. This observation is consonant with the idea that the central stalk enhances the efficiency of energy transduction, as has been suggested for the F_1–ATPase homologue.[15] Last, but certainly not least, our comparison of the free–energy landscapes mapped in the presence of and without the stalk indicates that energy dissipation is more prevalent in the isolated V_1–ring, relative to the full V_1–rotor. It follows that whereas the change in mechanical free energy is on the order of k_BT for the former, it increases to about 6 kcal/mol for the latter, germane to leverage the chemical work involved in hydrolysis.

Methods

Assessment of conformational transitions in proteins poses a serious computational challenge to brute–force MD simulations due to the virtual inaccessibility of micro– to millisecond timescales. Motor proteins, and V_1–ATPase in particular, raise this challenge even further to address the chemomechanical coupling between the ATP binding/hydrolysis sites and A_3B_3 proteins that characterizes the rotatory catalysis, while modeling these conformational transitions. With these challenges in mind, computational tools have been developed recently, combining several distinct path–optimization and enhanced–sampling techniques capable of describing large–scale protein conformational transitions in hexameric enzymes[30] and membrane transporters.[56]

Here, we address the aforementioned modeling and simulation challenges employing a two–step strategy. First, the central DF stalk of V_1–ATPase is removed and ATP–hydrolysis driven conformational transitions are examined only at the level of the A_3B_3 ring, denoted V_1-ring henceforth. Next, the DF stalk is reintroduced at every point along the A_3B_3 conformational transition pathway to capture the rotation of the stalk in concert with the

structural changes of the V_1–ATPase-ring, thereby allowing a comprehensive picture of rotatory catalysis in V_1–ATPase denoted V_1–rotor henceforth.

The two–step simulation strategy is summarized hereafter. First, the nucleotide (ATP and ADP + P_i) configurations within the three binding sites of V_1–ring, initially at state R^*, are manually assigned to set up a high–energy intermediate of A_3B_3, I^*, which follows from ATP hydrolysis (See Figure 2). The energy imparted to the system through the assignment of nucleotide configurations is measured in terms of binding affinity differences, employing alchemical transformations,[27] that is free–energy calculations aimed at altering chemical species. Since the RMSD between R^* and I^* is 0.3 Å in comparison to R^* and F^*, 4.5 Å the $R^* \rightarrow I^*$ transition invoke little mechanical work. Conformational rotation of the V_1–ring allows the chemically activated high–energy state to be relaxed back to the ground–state conformation. This relaxation pathway is captured utilizing a combination of path–searching algorithms based on anisotropic network modeling (ANM),[36] targeted molecular dynamics (TMD),[25] and the so–called string method.[26,37] In the second step, the central DF stalk is introduced within structures at each point along the V_1–ring trajectory employing TMD and molecular dynamics flexible fitting (MDFF) simulations.[57] These points are then connected by means of another round of string simulations to obtain a minimum free–energy pathway characterizing the rotatory catalysis of the V_1–rotor.

Free–energy changes are measured for both the V_1–ring and rotor conformational transition pathways employing bias–exchange umbrella sampling (BEUS) computations.[38,39,56] These free–energy changes provide a quantification of how much of the chemical energy arising from ATP hydrolysis is utilized in the conformational transitions as opposed to being thermally dissipated, elucidating, in turn, the energy conversion efficiency of the motor. Finally, rate measurements are performed with maximum–likelihood methods[28] as a route to access the turnover of ATP hydrolysis for direct comparison with single–molecule measurements of the V_1–rotor.[7]

In what follows, we first list the key MD simulation parameters that are utilized. Second, the alchemical free–energy calculations[27] aimed at the accurate estimation of binding affinities are described. Third, ANM and string simulation protocols[26,37] are introduced for computing the most probable transition path. Finally, the BEUS simulations,[38,39,56] and maximum-likelihood procedures[28] for the determination of conformational free–energy changes and rate constants are outlined. We note that the aggregate simulation time, including string simulations with swarm of trajectories,[26] enhanced sampling for free–energy and rate–kinetic calculations, and alchemical transformations amounts to nearly 65 μs (see Table S1).

Modeling and molecular dynamics simulations

The MD study is based on a crystal structure of the V_1–rotor from *Enterococcus hirae* (PDBID: 3VO6).[1] For simulation purposes, the artificial ATP mimetics, namely AMP-PNP, which are employed as inhibitors for isolating crystals, are replaced by real ATP molecules in the bound states (**b**) and in the vicinity of the empty state (**e**) to generate state $\mathbf{b}^-$, ADP and an inorganic phosphate (modeled as $H_2PO_4^-$) in the tight state (**t**), and removed in the (**t′**) state (Figure 2). Structural analyses[58] have demonstrated that non–hydrolyzable

AMP-PNP can successfully mimic the ATP and ADP + P_i binding states in F_1–ATPase; different ATP analogues produce in fact similar binding conformations.[58] The simulations are first performed without the stalk, only for the V_1–ring, and subsequently repeated for the entire V_1–rotor.

The V_1–ring and rotor are solvated respectively in water boxes of size 170 Å × 170 Å × 170 Å and 170 Å × 170 Å × 190 Å with 150 mM NaCl; the simulation system sizes are 0.36 M and 0.49 M atoms, respectively. After a 4,000–step energy minimization, the system is thermalized to 300 K in 50 ps at 1 atm, employing harmonic positional restraints with a 1 kcal/mol/$Å^2$ spring constant on heavy atoms. Keeping the same spring constant, a 1 ns equilibration in the isobaric–isothermal ensemble (1 atm at 300 K) is carried out, followed by a 4 ns canonical–ensemble simulation, gradually decreasing the spring constant to zero during the latter stage. In what follows, we refer to the state of the resulting V_1–ring as the intermediate state I^*, and that of the V_1–rotor as I (see Figures 1–2). All MD simulations in our study are performed using NAMD 2.10[59] with the CHARMM27 force field[60] and CMAP corrections.[61]

Alchemical transformations

The standard binding free energy of the nucleotides to the catalytic domain of the V_1–rotor is determined following a double-annihilation strategy,[62,63] wherein the substrate, either ATP or ADP + P_i, is decoupled reversibly from its environment, in the three bound states — i.e., tightly bound (t), bound (b) and empty (e), and in the free state. This strategy raises a conceptual difficulty rooted in the substantial change in the conformational, translational and rotational entropies associated to the binding process, which is not easily captured in classical MD simulations. Furthermore, as the substrate is progressively decoupled from the catalytic domain, it becomes free to wander away, resulting in an ill–defined target state and a poor starting point for the reverse, coupling transformation, prone to violate thermodynamic micro–reversibility.[64] To address cogently this issue, a series of geometrical restraints acting on collective variables are introduced to alleviate the sampling limitations of finite–length free-energy calculations (see Figure S2).[65,66] The contribution to the binding affinity arising from the loss of configurational entropy is estimated in separate simulations following the procedure described in reference 65. The alchemical transformations in the bound state and in the free state are carried out bidirectionally using free–energy perturbation (FEP).[41,42] The statistical information accrued in the forward and backward simulations is combined employing the Bennett acceptance ratio algorithm[67] to yield a maximum–likelihood estimator of the free energy. Decoupling of the substrate from its environment, in the enzyme and in the bulk medium, is stratified, respectively, in 500 windows, consisting each of 50 ps of thermalization followed by 200 ps of data collection. The choice of an appreciably large number of strata is dictated by the necessity of sampling from the reference state microstates representative of the target state.[68] The number of nonphysical intermediate states utilized here ensured appropriate overlap of the underlying ensembles of states (see supporting information). The length of the alchemical transformations from whence the ensemble averages are estimated amounted 125 ns per calculation. The contribution of the geometric restraints to the binding affinity is determined in two independent free–energy calculations, 7 ns long, in the bound state and in the free

state, respectively, bringing to 264 ns the total simulation time required to obtain the binding affinity of each substrate, either ATP or ADP + P_i, to the catalytic domain of V_1–rotor, in the three different binding modes (see summary in Table S2 of the supporting information). The error bar associated to the net free–energy changes is inferred from the hysteresis between the forward and the backward transformations. Detail of the different steps towards the final standard binding free energy can be found in the supporting information.

Anisotropic network modeling

Preliminary pathways probing transitions in the V_1–ring are constructed employing anisotropic network models (ANM).[36] An ANM trajectory employs harmonic spring approximations to provide the lowest potential energy transition pathway connecting two end states. Presented in Figure S3, seven ANM pathways are constructed at C–α resolution between the I^* and F^* states of the A_3B_3 protein: all the three protein-dimer states are allowed to change simultaneously in the first step, (A^eB^e, A^tB^t, $A^bB^b \rightarrow A^bB^b$, A^eB^e, A^tB^t); two protein-dimer states change simultaneously, (A^eB^e, A^tB^t, $A^bB^b \rightarrow A^bB^b$, A^eB^e, A^bB^b), (A^eB^e, A^tB^t, $A^bB^b \rightarrow A^eB^e$, A^eB^e, A^tB^t), (A^eB^e, A^tB^t, $A^bB^b \rightarrow A^bB^b$, A^tB^t, A^tB^t); only one dimer state changes at a time (A^eB^e, A^tB^t, $A^bB^b \rightarrow A^bB^b$, A^tB^t, A^bB^b), (A^eB^e, A^tB^t, $A^bB^b \rightarrow A^eB^e$, A^eB^e, A^bB^b), (A^eB^e, A^tB^t, $A^bB^b \rightarrow A^eB^e$, A^tB^t, A^tB^t). The product from the pathway with the lowest barrier among the seven ANM pathways, (A^eB^e, A^eB^e, A^bB^b), is subjected to two further transitions (A^eB^e, A^eB^e, $A^bB^b \rightarrow A^bB^b$, A^eB^e, A^bB^b) and (A^eB^e, A^eB^e, $A^bB^b \rightarrow A^eB^e$, A^eB^e, A^tB^t); the former pathway exhibits a smaller barrier. Thus, the final step involves a (A^bB^b, A^eB^e, $A^bB^b \rightarrow A^bB^b$, A^eB^e, A^tB^t) transition. Altogether, the pathway connecting I^* (A^eB^e, A^tB^t, A^bB^b) to F^* (A^bB^b, A^eB^e, A^tB^t) that exhibits the lowest barrier height follows the sequence of transitions: (A^eB^e, A^tB^t, $A^bB^b \rightarrow A^eB^e$, A^eB^e, A^bB^b) $\rightarrow$(A^eB^e, A^eB^e, $A^bB^b \rightarrow A^bB^b$, A^eB^e, A^bB^b) $\rightarrow$(A^bB^b, A^eB^e, $A^bB^b \rightarrow A^bB^b$, A^eB^e, A^tB^t). This pathway is characterized by 30 [see Figure S3 (c)] + 25 [see Figure S3 (d)] + 20 [number of models along the (A^bB^b, A^eB^e, $A^bB^b \rightarrow A^bB^b$, A^eB^e, A^tB^t) pathway]= 75 models in total. The lowest potential energy pathway is resolved at full–atomic detail via TMD simulations.[25] These simulations bias the trace of state I^* onto each one of the 75 models along the ANM pathway, while letting all other atoms in the structure relax, thus providing an all–atom trial pathway between I^* and F^*. This ANM–based TMD pathway is discretized into 100 equally distant milestones, termed images from here on, and optimized subsequently via string simulations, as described in the next section, to obtain a minimal free energy pathway (MFEP) for conformational rotation of the V_1–ring.

Next, the central stalk (DF subunit) is introduced into the MFEP for V_1–ring to construct a pathway that simultaneously captures the V_1–ring conformational rotation, as well as the physical rotation of the stalk within the entire V_1–rotor. To achieve this pathway, the A_3B_3 proteins in I of V_1–rotor are steered to the 100 conformations that were originally observed along each point of the aforementioned minimum free energy V_1–ring transition path. The steering specifically involves TMD simulations of the A_3B_3 proteins in V_1–rotor towards AB conformations from the V_1–ring transition path as target. Thus, a conformational rotation is induced within the A_3B_3 part of V_1–rotor connecting states I and F. Illustrated in Figure S4, the central stalk is modeled into these A_3B_3 conformations via flexibly fitting it, employing MDFF,[57] into the densities of the central pore of the V_1–ring. Because shape and

orientation of the pore changes with the conformational rotation in the V_1–ring proteins transitioning between I^* and R^*, the MDFF fitting allows both deformation and rotation of the stalk within the pore densities to gain maximal map–stalk cross–correlation (CC) at each of the 100 conformations. The MDFF–generated stalk placement is performed in concert with the TMD–imposed A_3B_3 conformational rotation, as part of a single simulation protocol of the V_1–rotor, so the AB and the stalk dynamics remain coupled while the latter rotates across the 100 conformations. Once the RMSDs with respect to the targets during 1–6 ns TMD simulations converge to a near–zero value, and the CCs to the map reach a maximum, the V_1–rotor conformations are refined again by means of string simulations. The entire simulation scheme is summarized in the workflow of Figure S5. The structural results from the string simulations are presented in Figures 3 and 5. The associated free–energy changes are provided in Figure 4.

String simulations

In the present study, we opted for the so–called string method with swarms of trajectories[26] to describe the roughly millisecond-scale $I^*/I \rightarrow F^*/F$ transition pathway, which is represented by a string/curve in a space of collective variables $\zeta(x)$, in which ζ is a n–dimensional function of atomic coordinates $\mathrm{x}(x \in \mathbb{R}^{3N})$, where $n << N$. The string is discretized into $M + 1$ equally spaced images, which are conformational states of V_1–ring and rotor along the I→F transition. Each of the M images is characterized by a n–dimensional collective variable $\zeta^{(M)}$. For the present case, $M = 99$ as obtained from the ANM–based pathways described above.

Due to the high dimensionality of the movement in the I→F transition we have to select ζ through a systematic computational procedure, as the large number of collective variables needed cannot be hand-picked. The collective variables suitable for the present case should describe the dominant changes that arise during the I→F transition. These collective variables are identified to be the positions of key residues at the six subunit-subunit interfaces of the AB trimer. The residue-based interaction energy contribution of AB interface are determined as shown in Figure S6, the energy as well as the interface RMSD serving as a collective variable selection criterion as explained in Supporting Information. From this procedure resulted eventually 393×3 = 1,179 coordinate positions, i.e, $n = 1{,}179$.

Ten replica of 0.35–ns long MD simulations are performed for each of the 100 images geometrically restrained to the instantaneous state of the 1,179 coordinate positions; a strong harmonic force constant of 50 kcal/mol/Å^2 is applied to restrain these positions. A swarm of short trajectories (20 × 25 ps) is launched subsequently from each image and the image evolves according to the average drift of its trajectory swarm during each iteration, followed by a reparametrization procedure, which enforces an equidistant distribution of images along the evolved string. The pathway is thus optimized iteratively until it converges to the most probable transition path, which is an approximate MFEP. The transition pathway for the V_1–ring took 50 iterations (Figure S7a) to converge while that of the V_1–rotor required 20 subsequent iterations (Figure S7b).

Our implementation of the string method[28] benefits from a scalable multiple copy algorithm of NAMD 2.10,[59] which enables launching thousands of trajectories simultaneously on a petascale supercomputer. The total simulation time needed for the sum of all string method trajectories amounts to 28 μs for the two pathways depicted in Figure 2.

Bias–exchange free energy calculations

Bias–exchange umbrella sampling (BEUS) simulations[38,39,56] are performed along the converged MFEP derived from the string simulations of the V_1–rotor conformational transitions to estimate the associated free energy changes when $\mathbf{X} = \mathbf{t}$ and $\mathbf{X} = \mathbf{t}'$. The BEUS simulations for both the pathways are performed employing 1,179 collective positions constrained to distinct values along the images derived from the MFEP. To ensure sufficient window overlap in BEUS simulations, the number of images is increased to 175; the first 75 images starting from state I are evenly interpolated to crate 150 points along the transition path, while the final 25 images are retained as is from the final string trajectory. An exchange is attempted every 1 ps between each image and one of its two nearest neighboring images in an alternating fashion. Ten replicas per image are employed for 8-ns long BEUS simulations. A force constant of 2 kcal/mol/Å^2 is employed per atom to restrain geometrically the position of the atoms in the course of the free energy calculations, which results in roughly similar rate of exchange rates between neighboring windows (ranging from 29% to 40%). Two 10 replicas / image × 175 images × 8 ns/replica = 14 μs BEUS simulations are performed for the construction of two one–dimensional free–energy profiles, taking up a total sampling time of 28 μs. The statistics collected in the course of this simulation is employed to construct probability and subsequently free energy changes using a maximum-likelihood scheme presented in reference 28, and also detailed in the Supporting Information.

In the BEUS scheme, samples generated by each umbrella are assumed to satisfy the detailed balance relation and have the correct (biased) Boltzmann distribution. However, the initial conformations are not always selected from the correct distribution. The timescale associated with relaxation of these conformations to a correct distribution, τ, is roughly estimated in ps, employing the relationship $\tau = (M^2 + 1)/(10r)$,[56] where M is the number of images in the string and r is the average exchange rate; here, $\tau = 2500$ ps. Thus, a sample size of 80 ns/image (8 ns/replica), which is an order of magnitude more than the relaxation time, is expected to provide a correct biased Boltzmann distribution for the restrained-ensemble. It is indeed the case as demonstrated in (Figure S8a).

Three different free–energy profiles are constructed with a maximum-likelihood procedure[56,69] (detailed in the Supporting Information), using the data from the BEUS simulations: V_1-ring with 1,179 collective variables, the latter representing 393 interface residues (Figure S6), V_1-rotor with 1,179 collective variables, and V_1-rotor with 1,179 + 6 × 3 = 1197 collective variables, which probe free energy changes from the aforementioned 393 interface residues, as well as those from 6 residues on the stalk [R14, R24, L28, R165, E180, R186 (Figure 6)].

Convergence of the free–energy calculation is tested for each of the three cases using a resampling protocol. 50% of the data is randomly chosen and two one–dimensional free

energy profiles are constructed employing the aforementioned maximum–likelihood method.[28] The process is repeated 100 times to obtain a collection of 200 PMFs. After these 100 trials a converged mean profile is obtained across the 200 PMFs, and the standard deviation is considered as the error estimate. An error bound of ±1.5 kcal/mol is estimated for our PMF calculations (Figure S8b).

Furthermore, validity of the stiff–spring approximation, under which the so–called perturbed free energy as estimated here approaches the PMF,[28] is tested by computing higher–order corrections of the one–dimensional free–energy profile. The higher order terms were negligible as compared to the statistical error discussed above, providing evidence for the validity of the stiff–spring approximation within the margin of error (Figure S8b).

Finally, it ought to be noted, that we do not use a 1,179–dimensional umbrella–sampling protocol to estimate the PMF. Instead, we perform a one–dimensional umbrella sampling simulation along an MFEP, which is defined as a curvilinear abscissa in a high–dimensional free–energy landscape of the V_1–rotor, where the one–dimensional model reaction coordinate is defined in terms of 1,179 collective variables. In the theoretical development provided in the Supporting Information, this model reaction coordinate is shown to be the arc-length of the MFEP.

Rate estimation

In order to estimate the transition rate, we need to estimate the position–dependent diffusion constant along the MFEP in addition to the already estimated PMF. We used a maximum–likelihood approach to estimate the diffusion constant at each discretized point along the MFEP, represented by a BEUS/string image. Therefore, free unbiased simulations are carried out, starting from each image and analyzed as discussed in detail in the Supporting Information. For each image i, 20 copies of unbiased simulations are performed starting from 20 initial conformations generated by the BEUS simulations for window i. Each unbiased simulation is run for 2 ns and all the collective variables are collected every 64 ps (i.e., the lag time Δt) to determine the current image index of the conformation and monitor the jumps between different images. Using 175 (number of images) × 20 (number of copies) unbiased trajectories, we estimate $N_{i,j}$ (number of observed jumps from image i to j). The diffusion constant $D(\xi_i)$ can be then estimated from N matrix using the iterative Monte Carlo algorithm discussed in supporting information. The mean first passage time, $\overline{\tau}_{FP}$, (i.e., the inverse rate, k^{-1}) from the initial (I) to the final (F) state can then be estimated using the relation (20) from the Supporting information.

Since these results are dependent on the lag time, Δt, we repeated all these steps for Δt = 2, 4, 8, 16, 32 and 64 ps (Figure S9c). Use of smaller lag times is found to overestimate the rate (due to the correlation of the data), while longer lag times (Δt = 32, 64 ps) result in consistently similar rates. We also calculated the autocorrelation time for the image–index time series, using all unbiased simulations, which was estimated to be ~68 ps (Figure S9d). It is, therefore, reasonable to assume that a lag time Δt = 64 ps is long enough to ensure that the data points used to estimate the diffusion constant and rate are not significantly correlated.

Supplementary Material

Refer to Web version on PubMed Central for supplementary material.

Acknowledgments

The research reported has been supported by the National Institute of Health through Grants 9P41GM104601 and R01-GM067887-11, and the National Science Foundation through Grants MCB1616590 and PHY1430124. The authors also acknowledge supercomputer time on Stampede provided by the Texas Advanced Computing Center (TACC) at the University of Texas at Austin through Extreme Science and Engineering Discovery Environment (XSEDE) Grants XSEDE MCA93S028. This research used resources of the Oak Ridge Leadership Computing Facility at the Oak Ridge National Laboratory, which is supported by the Office of Science of the U.S. Department of Energy under Contract No. DE-AC05-00OR22725. A.S. is grateful for financial support from the Beckman Foundation, and NSF through the Center for Physics of Living Cells.

References

1. Arai S, Saijo S, Suzuki K, Mizutani K, Kakinuma Y, Ishizuka-Katsura Y, Ohsawa N, Terada T, Shirouzu M, Yokoyama S, Iwata S, Yamato I, Murata T. Nature. 2013; 493:703–707. [PubMed: 23334411]
2. Mulkidjanian AY, Makarova KS, Galperin MY, Koonin EV. Nat Rev Microbiol. 2007; 5:892–899. [PubMed: 17938630]
3. Boyer PD. Annu Rev Biochem. 1997; 66:717–749. [PubMed: 9242922]
4. Boyer PD. Nature. 1999; 402:247–249. [PubMed: 10580491]
5. Boyer PD. Mol Cell. 2001; 8:246–247. [PubMed: 11545726]
6. Suzuki T, Tanaka K, Wakabayashi C, Saita EI, Yoshida M. Nat Chem Biol. 2014; 10:930–936. [PubMed: 25242551]
7. Nakano M, Imamura H, Toei M, Tamakoshi M, Yoshida M, Yokoyama K. J Biol Chem. 2008; 283:20789–20796. [PubMed: 18492667]
8. Yokoyama K, Ohkuma S, Taguchi H, Yasunaga T, Wakabayashi T, Yoshida M. J Biol Chem. 2000; 275:13955–13961. [PubMed: 10788522]
9. Abrahams JP, Leslie AG, Lutter R, Walker JE. Nature. 1994; 370:621–628. [PubMed: 8065448]
10. van Raaij MJ, Abrahams JP, Leslie AG, Walker JE. Proc Natl Acad Sci U S A. 1996; 93:6913–6917. [PubMed: 8692918]
11. Böckmann RA, Grubmüller H. Nat Struct Biol. 2002; 9:198–202. [PubMed: 11836535]
12. Senior AE, Nadanaciva S, Weber J. Biochim Biophys Acta. 2002; 1553:188–211. [PubMed: 11997128]
13. Börsch M, Diez M, Zimmermann B, Reuter R, Gräber P. FEBS Lett. 2002; 527:147–152. [PubMed: 12220651]
14. Mukherjee S, Warshel A. Proc Natl Acad Sci U S A. 2015; 112:2746–2751. [PubMed: 25730883]
15. Czub J, Grubmüller H. J Am Chem Soc. 2014; 136:6960–6968. [PubMed: 24798048]
16. Okazaki K, Hummer G. Proc Natl Acad Sci U S A. 2015; 112:10720–10725. [PubMed: 26261344]
17. Pu J, Karplus M. Proc Natl Acad Sci U S A. 2008; 105:1192–1197. [PubMed: 18216260]
18. Ito Y, Oroguchi T, Ikeguchi M. J Am Chem Soc. 2011; 133:3372–3380. [PubMed: 21341660]
19. Uchihashi T, Iino R, Ando T, Noji H. Science. 2011; 333:755–758. [PubMed: 21817054]
20. Czub J, Grubmüller H. Proc Natl Acad Sci U S A. 2011; 108:7408–7413. [PubMed: 21502534]
21. Junge W, Sielaff H, Engelbrecht S. Nature. 2009; 459:364–370. [PubMed: 19458712]
22. Adachi K, Oiwa K, Nishizaka T, Furuike S, Noji H, Itoh H, Yoshida M, Ki-nosita K Jr. Cell. 2007; 130:309–321. [PubMed: 17662945]
23. Nam K, Pu J, Karplus M. Proc Natl Acad Sci U S A. 2014; 111:17851–17856. [PubMed: 25453082]
24. Das A, Gur M, Cheng MH, Jo S, Bahar I, Roux B. PLoS Comput Biol. 2014; 10:e1003521. [PubMed: 24699246]

25. Schlitter J, Engels M, Krüger P. J Mol Graph. 1994; 12:84–89. [PubMed: 7918256]
26. Pan AC, Sezer D, Roux B. J Phys Chem B. 2008; 112:3432–3440. [PubMed: 18290641]
27. Chipot C. Wiley Interdiscip Rev Comput Mol Sci. 2014; 4:71–89.
28. Moradi M, Enkavi G, Tajkhorshid E. Nat Commun. 2015; 6:8393. [PubMed: 26417850]
29. Hummer G. New J Phys. 2005; 7:34.
30. Ma W, Schulten K. J Am Chem Soc. 2015; 137:3031–3040. [PubMed: 25646698]
31. Furuike S, Nakano M, Adachi K, Noji H, Kinosita K Jr, Yokoyama K. Nat Commun. 2011; 2:233. [PubMed: 21407199]
32. Okazaki K, Hummer G. Proc Natl Acad Sci U S A. 2013; 110:16468–16473. [PubMed: 24062450]
33. Minagawa Y, Ueno H, Hara M, Ishizuka-Katsura Y, Ohsawa N, Terada T, Shirouzu M, Yokoyama S, Yamato I, Muneyuki E, Noji H, Murata T, Iino R. J Biol Chem. 2013; 288:32700–32707. [PubMed: 24089518]
34. Hayashi S, Ueno H, Shaikh AR, Umemura M, Kamiya M, Ito Y, Ikeguchi M, Komoriya Y, Iino R, Noji H. J Am Chem Soc. 2012; 134:8447–8454. [PubMed: 22548707]
35. Ueno H, Minagawa Y, Hara M, Rahman S, Yamato I, Muneyuki E, Noji H, Murata T, Iino R. J Biol Chem. 2014; 289:31212–31223. [PubMed: 25258315]
36. Eyal E, Yang LW, Bahar I. Bioinformatics. 2006; 22:2619–2627. [PubMed: 16928735]
37. E W, Ren W, Vanden-Eijnden E. Phys Rev B. 2002; 66:052301.
38. Neale C, Rodinger T, Pomès R. Chem Phys Lett. 2008; 460:375–381.
39. Jiang W, Phillips J, Huang L, Fajer M, Meng Y, Gumbart JC, Luo Y, Schulten K, Roux B. Comput Phys Comm. 2014; 185:908–916.
40. Moradi M, Tajkhorshid E. J Phys Chem Lett. 2013; 4:1882–1887. [PubMed: 23795244]
41. Landau, LD. Statistical physics. The Clarendon Press; Oxford: 1938.
42. Zwanzig RW. J Chem Phys. 1954; 22:1420–1426.
43. Senior AE. J Bioenerg Biomembr. 1992; 24:479–484. [PubMed: 1429542]
44. Gao YQ, Yang W, Marcus RA, Karplus M. Proc Natl Acad Sci U S A. 2003; 100:11339–11344. [PubMed: 14500780]
45. Kleinekathöfer U, Israelewitz B, Dittrich M, Schulten K. J Phys Chem A. 2011; 115:7267–7274. [PubMed: 21452901]
46. Yasuda R, Masaike T, Adachi K, Noji H, Itoh H, Kinosita K Jr. Proc Natl Acad Sci U S A. 2003; 100:9314–9318. [PubMed: 12876203]
47. Murata, T. (private communication).
48. http://robetta.bakerlab.org/alascansubmit.jsp,.
49. Dittrich M, Schulten K. J Bioenerg Biomembr. 2005; 37:441–444. [PubMed: 16691480]
50. Beke-Somfai T, Lincoln P, Nordén B. Proc Natl Acad Sci U S A. 2013; 110:2117–2122. [PubMed: 23345443]
51. Al-Shawi MK, Ketchum CJ, Nakamoto RK. Biochemistry. 1997; 36:12961–12969. [PubMed: 9335556]
52. Nakamoto RK, Baylis-Scanlon JA, Al-Shawi MK. Arch Biochem Biophys. 2008; 476:43–50. [PubMed: 18515057]
53. Chiwata R, Kohori A, Kawakami T, Shiroguchi K, Furuike S, Adachi K, Sutoh K, Yoshida M, K K Jr. Biophys J. 2014; 106:2166–2174. [PubMed: 24853745]
54. Wang H, Oster G. Nature. 1998; 396:279–282. [PubMed: 9834036]
55. Kinosita K Jr, Adachi K, Itoh H. Annu Rev Biophys Biomol Struct. 2004; 33:245–268. [PubMed: 15139813]
56. Moradi M, Tajkhorshid E. J Chem Theory Comput. 2014; 10:2866–2880. [PubMed: 25018675]
57. Trabuco LG, Villa E, Mitra K, Frank J, Schulten K. Structure. 2008; 16:673–683. [PubMed: 18462672]
58. Hong S, Pedersen PL. Microbiol Mol Biol Rev. 2008; 72:590–641. [PubMed: 19052322]
59. Phillips JC, Braun R, Wang W, Gumbart J, Tajkhorshid E, Villa E, Chipot C, Skeel LRDKalé, Schulten K. J Comput Chem. 2005; 26:1781–1802. [PubMed: 16222654]

60. MacKerell AD Jr, et al. J Phys Chem B. 1998; 102:3586–3616. [PubMed: 24889800]
61. Feig M, MacKerell AD, Brooks CL III. J Phys Chem B. 2003; 107:2831–2836.
62. Jorgensen WL, Buckner JK, Boudon S, Tirado-Rives J. J Chem Phys. 1988; 89:3742–3746.
63. Gilson MK, Given JA, Bush BL, McCammon JA. Biophys J. 1997; 72:1047–1069. [PubMed: 9138555]
64. Hermans J, Wang L. J Am Chem Soc. 1997; 119:2707–2714.
65. Gumbart JC, Roux B, Chipot C. J Chem Theor Comput. 2013; 9:794–802.
66. Gumbart JC, Roux B, Chipot C. J Chem Theor Comput. 2013; 9:3789–3798.
67. Bennett CH. J Comp Phys. 1976; 22:245–268.
68. Pohorille A, Jarzynski C, Chipot C. J Phys Chem B. 2010; 114:10235–10253. [PubMed: 20701361]
69. Bartels C. Chem Phys Lett. 2000; 331:446–454.

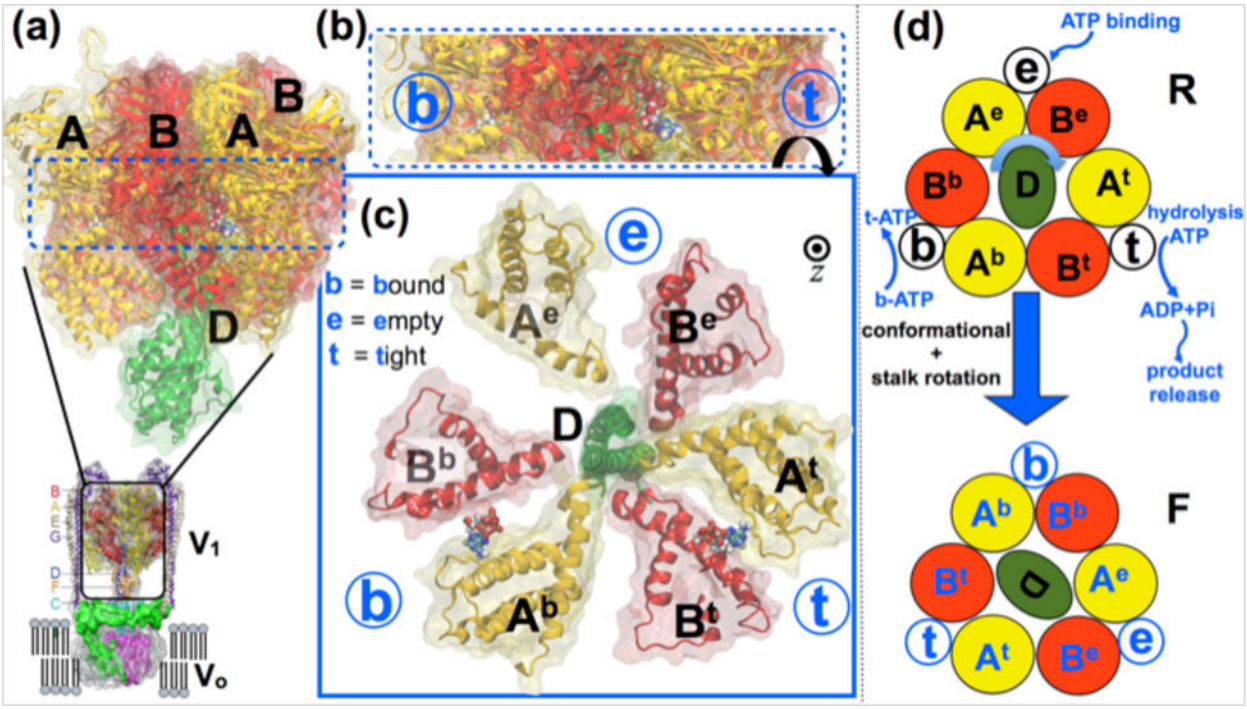

Figure 1. Structure and proposed rotatory catalysis mechanism of V_1–ATPase

(a) Zoom–out of the V_1 rotor of a V_oV_1–ATPase composed of three A (shown in yellow), three B (red) and one D (green) subunit. (b) Side–view of a transverse section of the V_1 rotor showing nucleotide (ATP/ADP) binding sites at the interface of the A and B subunits. (c) A top–down view of the transverse section in 1b showing three nucleotide binding sites at the AB interface and three other non-nucleotide-binding interfaces. The binding sites are labeled according to the state of nucleotide at the respective sites, namely, tight (**t**) where the ATP is hydrolysis-competent, bound (**b**) where the ATP is loaded into the binding pocket and does not have reached yet the reactive configuration, and empty (**e**) state that is devoid of nucleotide. Proteins in a particular binding site are denoted employing the site nomenclature, e.g., the tight site is composed of proteins in conformation denoted A^t and B^t and similarly for A^b and B^b in the bound state, and A^e and B^e in the empty state. (d) Proposed rotatory catalysis mechanism of V_1–rotor accompanying ATP hydrolysis. In binding ATP, releasing ADP + P_i and hydrolyzing ATP to ADP, the pattern of ligand binding sites corresponding to the protein surface conformations in a prior state R, A^eB^e (**e**), A^tB^t (**t**), A^bB^b (**b**), shifts to the final state F, A^bB^b (**b**), A^eB^e (**e**), A^tB^t (**t**). As one can easily recognize, the ligand binding sites and associated AB protein conformations of R, after a 120°clockwise rotation around the *z*–axis, are the same as those of F; but the moment of inertia of this conformational rotation of A_3B_3 is near zero. In contrast, going from R to F, the D subunit (central stalk) is also rotated by 120°. Thus, the latter rotation carries a significant moment of inertia of the stalk.

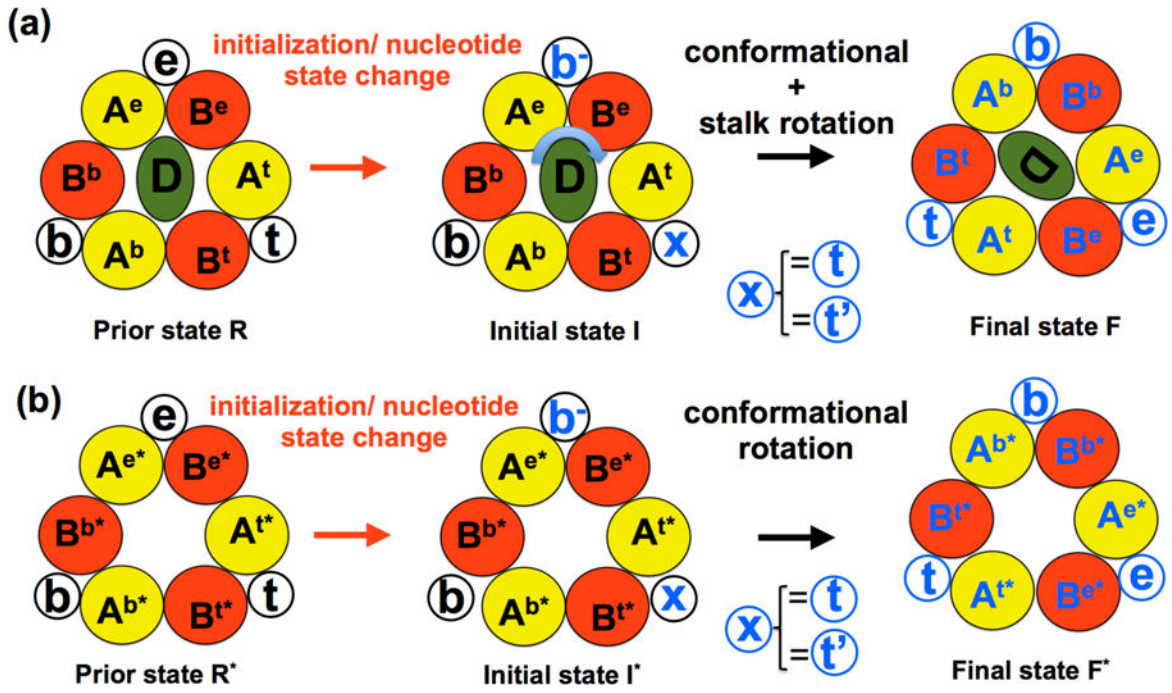

Figure 2. Rotatory reaction scheme

(a) Details of how states R, I, and F for the V_1–rotor (A_3B_3DF) have been constructed are described in Methods. The site $\mathbf{b}^-$ implies an empty, **e**, site with an ATP placed in the vicinity of the ATP–binding residues. The ligand state **X** at the interface between subunits A^t and B^t is assumed to be either the product bound tight site **t** (product not erased) or the state $\mathbf{t}'$ with proteins in the A^t and B^t conformation in site **e** (product released). (b) The calculations for (a) are repeated without the central stalk, D and F subunits included. To denote the absence of the stalk protein, subunits A and B are now designated with an asterisk (*). Initial nucleotide binding states are designated by black circles while the final binding states are designated by blue circles.

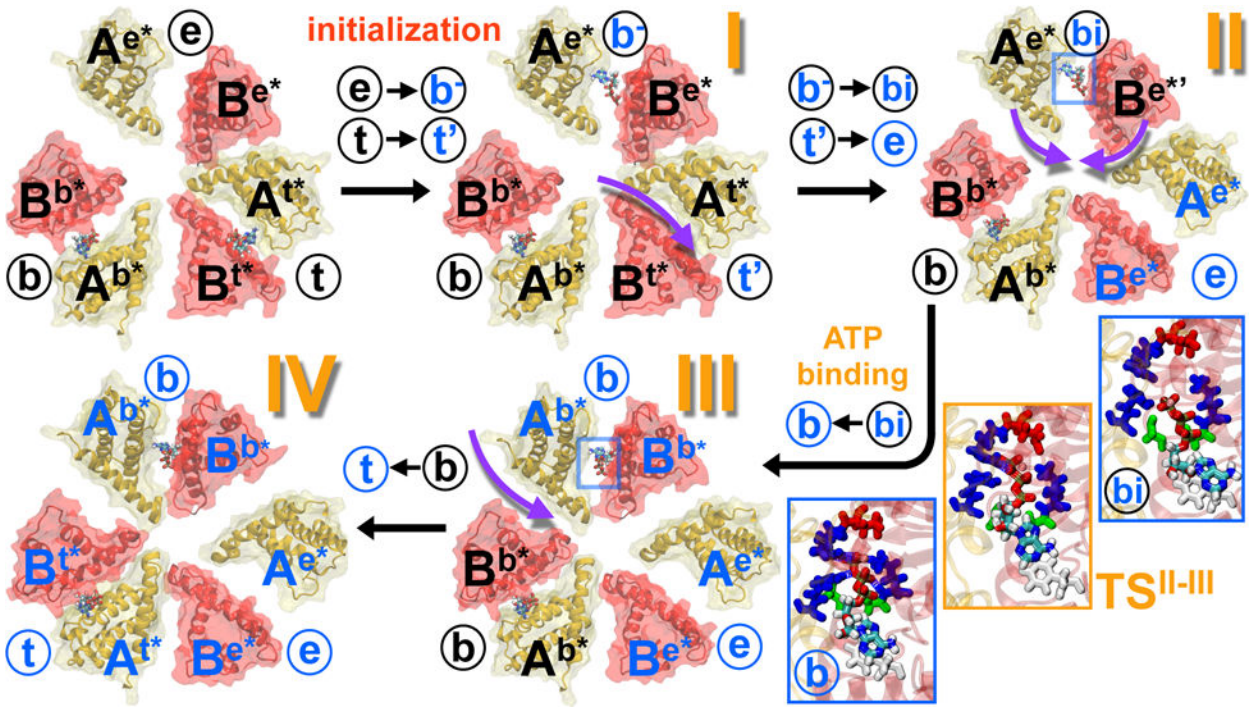

Figure 3. V_1–ring conformational rotation mechanism

Pathway of the hydrolysis-driven conformational transition in the V_1–ring complex of V_1–rotor derived from the string method with swarms of trajectory.[26] State R^* is first initialized to derive I^* according to the scheme in Figure 2b. The ensuing sequence of events implies transition from a tight (**t**) to an empty (**e**) conformation in the ADP+P_i–bound site (I^* II), promotes for ATP binding at the neighboring loosely–bound (**b**$^-$)site (II → III). Subsequently, a bound ATP in→the third site transitions to a reaction mode forming a new tight (**t**) conformation where it interacts with residue E261 that promotes hydrolysis (III → F^*). (inset) The ATP binding event accompanying the II → III transition exhibits a key transition barrier pertaining to the disruption of linkages between ATP's terminal phosphate group (including a Mg^{2+} ion (pink sphere)) and the positively charged side chain of the gate–keeper R350 residue from B^e that are overcome to allow the ATP inside the binding pocket for interacting with all the nucleotide-bindable residues, namely G235, G237, K238 and R262 (Figure S10).

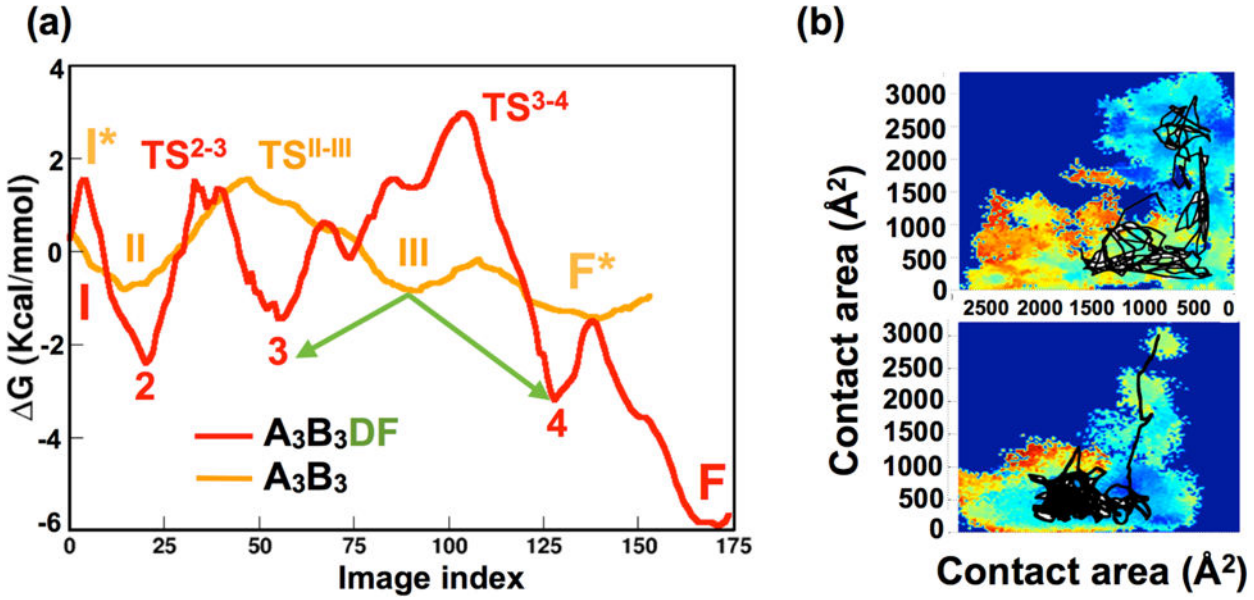

Figure 4. Free energy analysis of conformational transition

(a) One-dimensional free energy profiles along the ATP hydrolysis driven conformational transition pathways of the V_1–ring (orange) and V_1–rotor (red); while the pathways are deduced with the string method[26] based on 100 milestones (or images) characterizing the transition, the energy profile is computed employing BEUS[40] across 175 such images (see Methods). Detailed error-analysis is provided in Figure S8. Since the RMSD change between the last and the first image on the pathway is greater for the rotor than that for the ring, even with the same number of collective variables (Figure S6), the image indices of the ring are scaled with respect to the rotor, so that the corresponding free–energy profiles can be compared on the same plot. This scaling is achieved by multiplying each image index, i, of the ring–pathway with a factor *f*, where *f* = (RMSD of image i wrt image 0 on the ring pathway)/(RMSD of image i wrt image 0 on the rotor pathway). This scaling is possible because the string is derived in the Cartesian space, where the RMSD indeed provides an absolute measure of the Euclidean distance between two points, and allows the distance traversed along the ring pathway to be cast as a fraction of that along the rotor pathway. A free–energy change of about −2 kcal/mol is measured for the V_1–ring transition with two intermediates, II and III, independently isolated from X-ray crystallography, as illustrated in Figure S11. The major barrier involving ATP binding between intermediates II and III amounts to +2 kcal/mol. Introduction of the central stalk, DF, magnifies the depth of the minima, enhances the barrier heights, as well as makes the rotatory reaction thermodynamically more feasible, with a net free–energy change of about −6 kcal/mol. In addition, the V_1–rotor pathway includes one more intermediate than the V_1–ring transition pathway. (**b**) Two dimensional plot of the free–energy changes projected onto the contact area of the two transitioning AB interfaces, $A^tB^t \rightarrow A^eB^e$ interface along the *x*–axis and that of $A^eB^e \rightarrow A^bB^b$ along the *y*–axis; the superscript * is dropped from the AB notation here to allow the use of same nomenclature for the V_1–ring (upper panel) *vs* -rotor (lower panel) comparison. The black trace represents conformations of the swarms along the converged minimum energy pathway joining states I and F. Both the (A^tB^t, A^eB^e) and (A^eB^e, A^bB^b)

were accessible during the V_1–ring transition, implying their similarity in energy. However, most of the population contributes to the (A^eB^e, A^bB^b) state in the V_1–rotor, indicating a strong thermodynamic drive for rotation of the stalk as generated at the AB interface following ATP hydrolysis and product release.

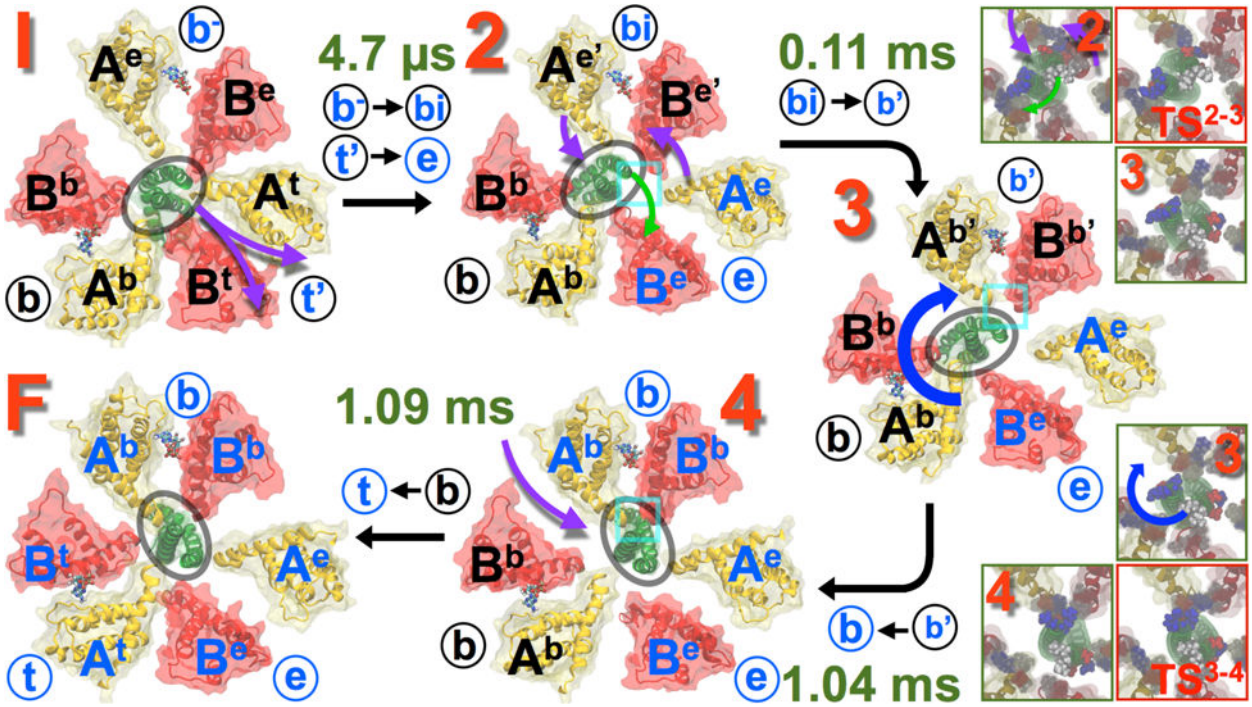

Figure 5. V_1–rotor conformational transitions mechanism

Pathway of the hydrolysis-driven conformational transition in the entire V_1–rotor derived from the string method with swarms of trajectories.[26] State R is first initialized to drive I according to Figure 2a. The ensuing sequence of events closely follows those of the V_1–ring presented in Figure 3. First, transition from a tight (**t**) to an empty (**e**) conformation (I → 2) is observed at the ADP+P_i-bound site. This transition promotes ATP binding at the neighboring $\mathbf{b}^-$-site, yielding the first doubly-bound (**b′**,**e**,**b**) state (2 → 3); the ATP binding simultaneously induces a local deformation of the central stalk. The stalk then rotates yielding the second doubly-bound (**b,e,b**) state (3 → 4). Finally, a bound ATP (**b**) in the third site transitions to a reaction mode in the tight (**t**) conformation, where it interacts with the E261 residue that promotes hydrolysis (4 → F). Rates of each of these transitions are computed employing techniques described in the Methods and supporting information, and labeled along with each step (Figure S9). The rotation step is found to be the slowest when it follows product release. (Upper inset) Transformation of an $A^{e'}B^{e'}$ interface to $A^{b'}B^{b'}$ during the 2 → 3 transition necessitates a wringe deformation of the stalk that marginally exposes hydrophobic residues L28 to water (also presented in Figure S19). This unfavorable solvation characterizes the first TS (TS^{23}), following which L28 re-establishes hydrophobic contacts with L385 of A^e and L477 of the second A^b. (Lower inset) Salt bridges between residues E161, R164 and R165 of the stalk and E472 and R475 of the $A^{b'}$ domain and E384 and $B^{b'}$ domains reorganize during the stalk-rotation step, involving transient repulsive electrostatic interactions of residues E161 and R164 (DF), with E472 and R475 ($A^{b'}$), respectively. These repulsive interactions characterize the second TS (TS^{34}), featuring the highest barrier of the V_1–rotor pathway. See also Figure S16 and movies (M1 to M6) in the Supporting Information showcasing details of the I → F transition from four different camera-angles.

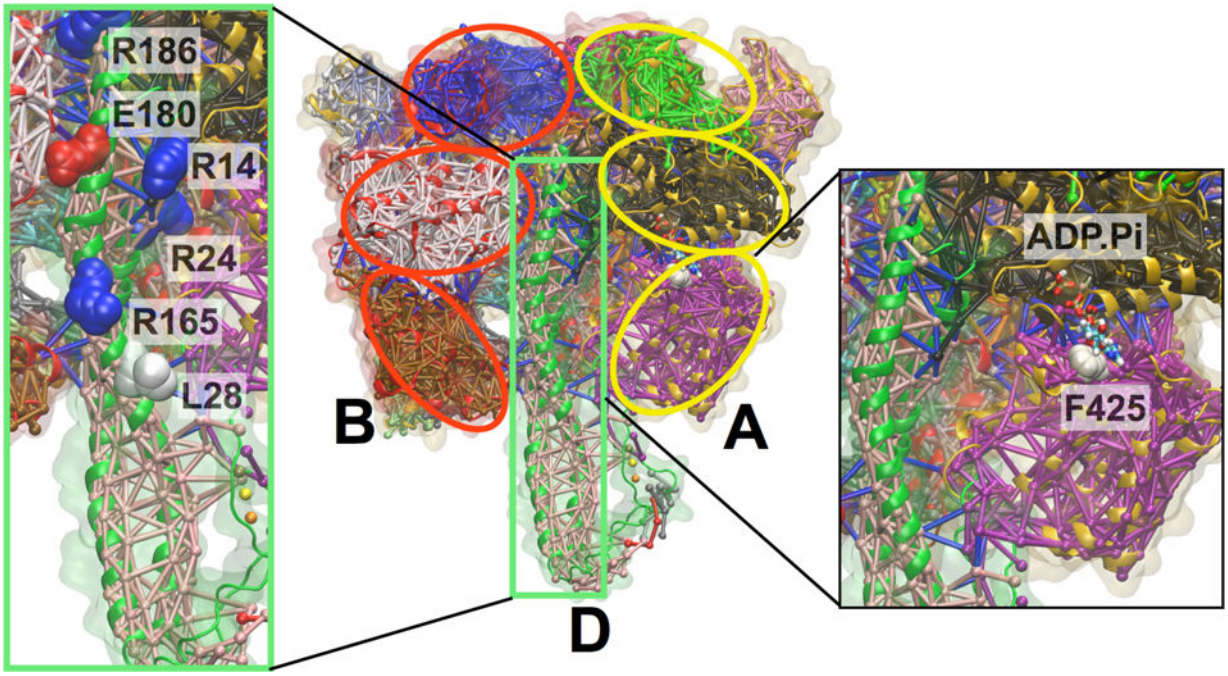

Figure 6. Correlated subunits of V_1–rotor

Network analysis of the V_1–rotor showing key dynamically correlated subunits of the V_1–ring and the DF stalk. Each of the A and B domains are composed of three subunits; the stalk is one correlated unit. (left inset) Residues on the DF stalk lining the correlation paths joining the stalk and the A domain. These residues are key to describe the ring-stalk allostery described below in Figure 9 and Figure 10. (right inset) Residues F425 at the margin of the lower two correlated subunits of the A domain also contributes to the ATP binding pocket π–π stacking with the adenine base. Thus, conformational changes of the F425 residue are expected to be coupled allosterically to the hinge-like motion between these two subunits.

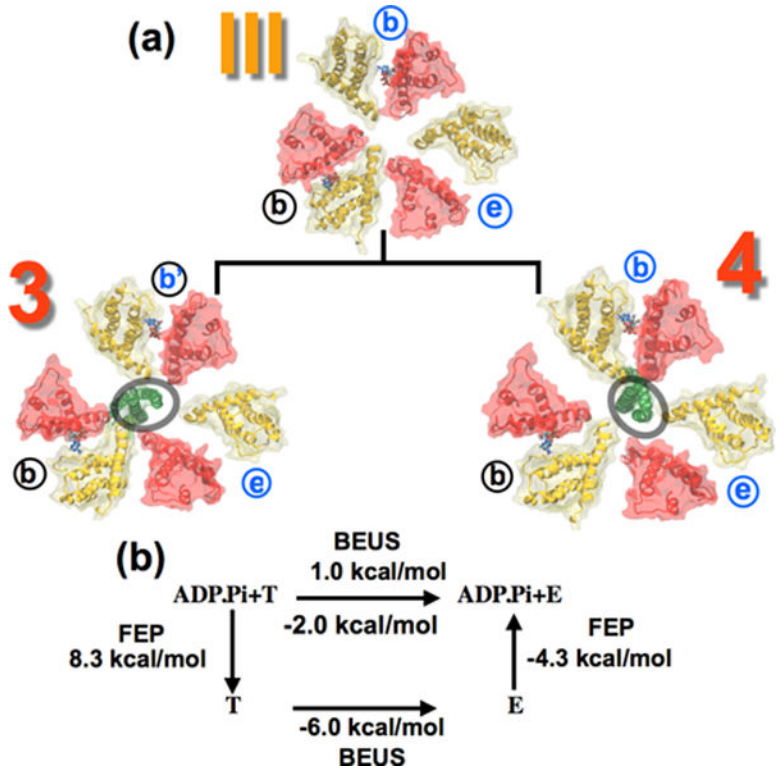

Figure 7. V_1–ring conformational–state degeneracy

(a) Top-down view of state II along the V_1–ring conformational transition pathway and states 3 and 4 along the V_1–rotor conformational transition showing that the **b,e,b** ring conformation can hold the DF stalk in two distinct conformations, namely, in the wrung and in the rotated forms (b) Thermodynamic cycle showing the free energy change due to conformation transition of the proteins computed via BEUS simulations is commensurate to alternations in the binding affinities computed from FEP calculations. There remains a reasonable hysteresis of 3 kcal/mol, however, it remains within the cumulative limits of the BEUS and FEP convergence errors reported in the supporting information. The FEP energies are reported in Table 1, while the BEUS energies are reported in Figures S13 (ADP.Pi + T ⟶ ADP.Pi + E, i.e., when **X** = **t** in Figure 2a) and 4a (T ⟶ E, when **X** = **t**′ in Figure 2a)

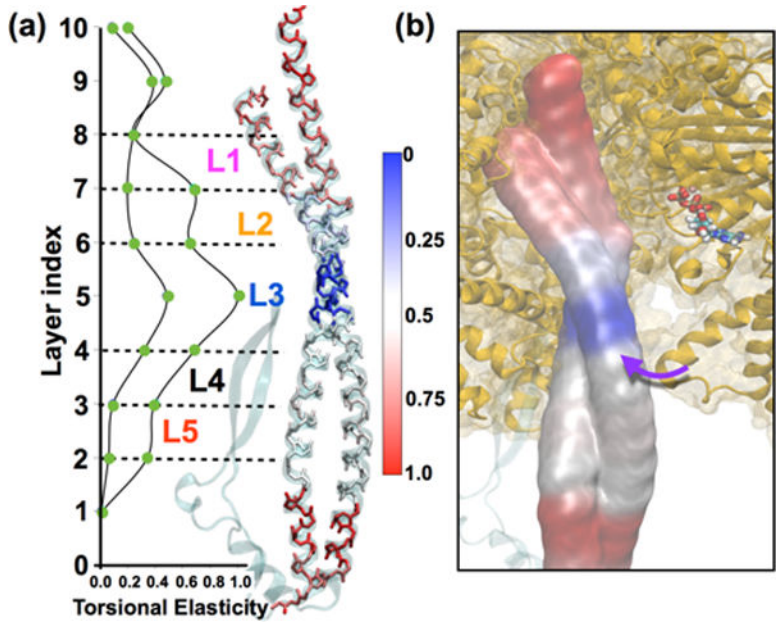

Figure 8. Torsional elasticity of DF stalk

(a) The DF stalk is colored by torsional elasticity, normalized on a scale of red (0.0) to blue (1.0), showing the central part of the stalk is most rigid and flexibility increases towards the termini. Plotted along the stalk are normalized torsional elasticities both in the presence and absence of the V_1–ring; the ring-interacting stalk is more rigid than an isolated stalk, yet the qualitative elasticity distribution remain unchanged suggesting that this distribution is intrinsic to the stalk. Based on the nature of elasticity the stalk is stratified into five layers L1 to L5. (b) The stalk, colored by elasticity, interacts with the A domain of the V_1–ring via a region of intermediate elasticity suggesting the flexibility of the stalk can be leveraged thermodynamically or kinetically to enable rotation of the stalk.

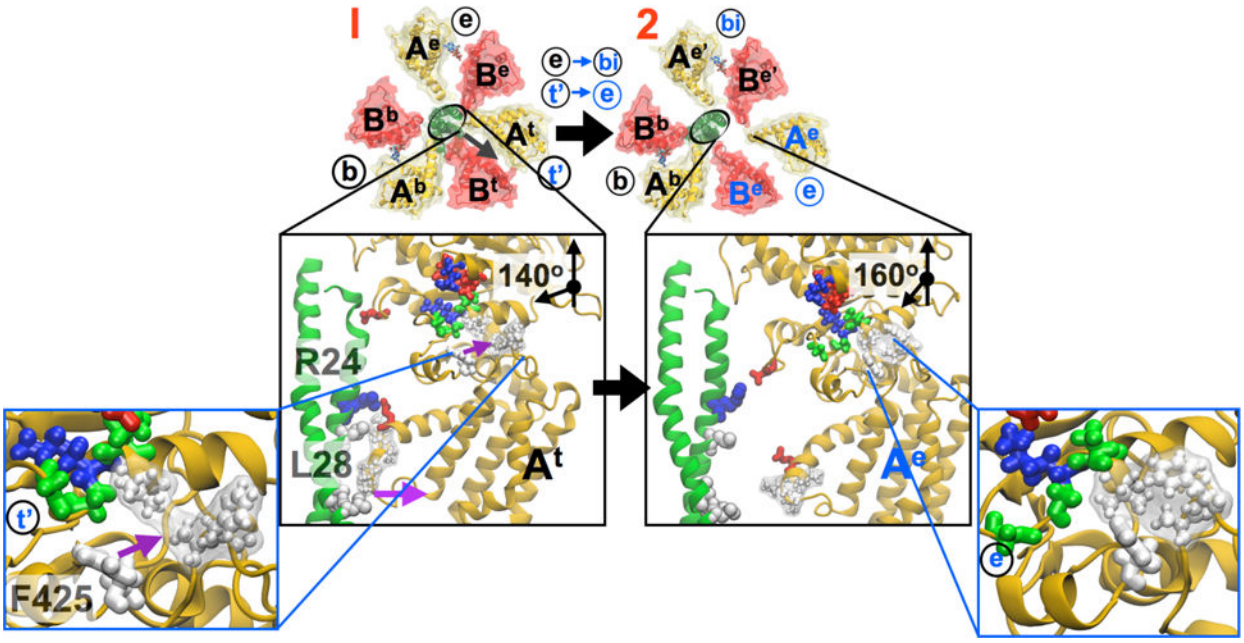

Figure 9. Ring-stalk allostery: I → 2 transition

Outward swivel of the A domain, by 20°, during the $A^t \rightarrow A^e$ transition is allosterically coupled to the motion of F425 in the ATP binding pocket (inset) as was suggested by the dynamical networks presented in Figure 6. Also, hydrophobic residues originally lining the stalk–A^t contact cluster to prevent exposure to water, and, the salt bridge between residues R24 of the stalk and E472 of A^t is replaced by the interaction of R24 with E396. All positively charged residues are indicated in red, positively charged residues in blue, and neutral residues in white. Charged residues from the V_1–ring are presented in licorice, with the neutral ones with an additional density representing solvent accessibility; residues on the stalk are presented in van der Waals representation. The same presentation is used in Figure 9 and Figure 10 For the sake of clear presentation only stalk residues are labeled in the figure; all key residues at the ring-stalk interface are illustrated in Figure S16

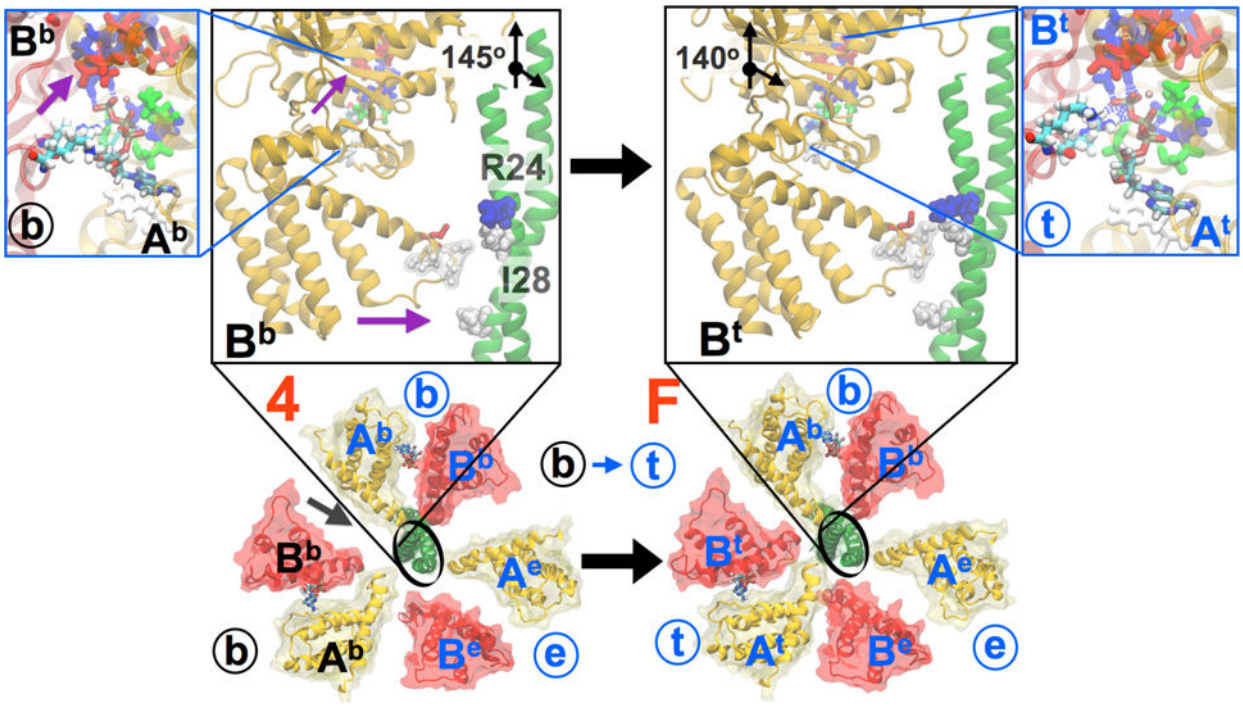

Figure 10. Ring-stalk allostery: 4 → F transition

Inward swivel of the A domain, by 15°, during the $A^b \rightarrow A^t$ reinstates the salt-bridge interactions between R24 from the stalk and E472 from A^t. The inward swivel allows deeper penetration of the ATP and the Mg^{2+} ion into the binding site allowing now interaction of the terminal phosphate with the E261 residue as required for subsequent hydrolysis reaction.

Table 1

Summary of the standard binding free–energy calculations performed for ATP and ADP+P_i bound to the catalytic domain of V_1–rotor.

Contribution	free–energy change (kcal/mol)	
	V_1–ATPase	F_1–ATPase[a]
ATP, tightly bound (t)		
$\Delta G^{\circ}_{\mathrm{bind}}$	**−11.6 ± 0.8**	−13.24
ATP, bound (b)		
$\Delta G^{\circ}_{\mathrm{bind}}$	**−8.9 ± 1.1**	−9.96
ATP, empty (e)		
$\Delta G^{\circ}_{\mathrm{bind}}$	**−4.1 ± 1.1**	−6.08
ADP+P_i, tightly bound (t)		
$\Delta G^{\circ}_{\mathrm{bind}}$	**−8.3 ± 0.9**	−6.19
ADP+P_i, empty (e)		
$\Delta G^{\circ}_{\mathrm{bind}}$	**−4.3 ± 0.8**	−6.49

[a] experimental estimate from reference 43.